Redox Biology 68 (2023) 102957

Contents lists available at ScienceDirect

Redox Biology

journal homepage: www.elsevier.com/locate/redox

Enhanced fatty acid oxidation through metformin and baicalin as therapy for COVID-19 and associated inflammatory states in lung and kidney

Verónica Miguel [a,j,*], Carlos Rey-Serra [a], Jessica Tituaña [a], Belén Sirera [a], Elena Alcalde-Estévez [a], J. Ignacio Herrero [a], Irene Ranz [a], Laura Fernández [a], Carolina Castillo [b], Lucía Sevilla [c], James Nagai [d,e], Katharina C. Reimer [f,g], Jitske Jansen [f,h], Rafael Kramann [f], Ivan G. Costa [d,e], Ana Castro [i], David Sancho [j], José Miguel Rodríguez González-Moro [c], Santiago Lamas [a,**]

[a] Program of Physiological and Pathological Processes, Centro de Biología Molecular "Severo Ochoa" (CBMSO) (CSIC-UAM), Madrid, Spain
[b] Department of Pathology. University Hospital "Príncipe de Asturias", Alcalá de Henares, Madrid, Spain
[c] Department of Pneumology, University Hospital "Principe de Asturias", Alcala de Henares, Madrid, Spain
[d] Institute for Computational Genomics, RWTH Aachen University Hospital, Aachen, Germany
[e] Joint Research Center for Computational Biomedicine, RWTH Aachen University Hospital, Aachen, Germany
[f] Department of Medicine 2, Nephrology, Rheumatology and Immunology, RWTH Aachen University, Medical Faculty, Aachen, Germany
[g] Institute for Biomedical Technologies, Department of Cell Biology, RWTH Aachen University, Aachen, Germany
[h] Department of Pathology, Radboud Institute for Molecular Life Sciences, Radboud University Medical Center, Nijmegen, the Netherlands
[i] Instituto de Química Medica (IQM-CSIC), Juan de la Cierva 3, 28006, Madrid, Spain
[j] Centro Nacional de Investigaciones Cardiovasculares Carlos III (CNIC), 28029, Madrid, Spain

ARTICLE INFO

Keywords:
Fibrosis
Metabolism
Mitochondria
Inflammation
COVID-19

ABSTRACT

Progressive respiratory failure is the primary cause of death in the coronavirus disease 2019 (COVID-19) pandemic. It is the final outcome of the acute respiratory distress syndrome (ARDS), characterized by an initial exacerbated inflammatory response, metabolic derangement and ultimate tissue scarring. A positive balance of cellular energy may result crucial for the recovery of clinical COVID-19. Hence, we asked if two key pathways involved in cellular energy generation, AMP-activated protein kinase (AMPK)/acetyl-CoA carboxylase (ACC) signaling and fatty acid oxidation (FAO) could be beneficial. We tested the drugs metformin (AMPK activator) and baicalin (CPT1A activator) in different experimental models mimicking COVID-19 associated inflammation in lung and kidney. We also studied two different cohorts of COVID-19 patients that had been previously treated with metformin. These drugs ameliorated lung damage in an ARDS animal model, while activation of AMPK/ACC signaling increased mitochondrial function and decreased TGF-β-induced fibrosis, apoptosis and inflammation markers in lung epithelial cells. Similar results were observed with two indole derivatives, IND6 and IND8 with AMPK activating capacity. Consistently, a reduced time of hospitalization and need of intensive care was observed in COVID-19 patients previously exposed to metformin. Baicalin also mitigated the activation of pro-inflammatory bone marrow-derived macrophages (BMDMs) and reduced kidney fibrosis in two animal models of kidney injury, another key target of COVID-19. In human epithelial lung and kidney cells, both drugs improved mitochondrial function and prevented TGF-β-induced renal epithelial cell dedifferentiation. Our results support that favoring cellular energy production through enhanced FAO may prove useful in the prevention of COVID-19-induced lung and renal damage.

1. Introduction

COVID-19 may affect almost any organ of the human body due to the wide distribution of peptidase angiotensin-converting enzyme 2 (ACE2), whose interaction with the virus spike protein S dictates its tropism [1]. Lung disease is by far the most important condition responsible for COVID-19 morbidity and mortality [2]. Once the virus infects epithelial

* Corresponding author. Centro Nacional de Investigaciones Cardiovasculares Carlos III (CNIC), 28029, Madrid, Spain.
** Corresponding author. Centro de Biología Molecular Severo Ochoa, Calle Nicolás Cabrera 1, Madrid, 28049, Spain.
E-mail addresses: veronica.miguel@cnic.es (V. Miguel), slamas@cbm.csic.es (S. Lamas).

https://doi.org/10.1016/j.redox.2023.102957
Received 25 September 2023; Received in revised form 1 November 2023; Accepted 1 November 2023
Available online 3 November 2023

cells from the upper respiratory tract, it may evolve to symptomatic pneumonitis by infecting ACE2-expressing type 2 alveolar epithelial cells. In a later phase, severe disease may develop, involving disruption of the epithelial-endothelial barrier, complement deposition and an acute inflammatory reaction with a massive release of cytokines [3], causing diffuse alveolar damage and respiratory insufficiency, often refractory to therapy [4]. This state shares most of the molecular and pathophysiological features of acute respiratory distress syndrome (ARDS), which may be caused by an ample spectrum of infectious and non-infectious agents. ARDS remains a major clinical challenge as mortality in severe ARDS is close to 50% and many patients who survive it suffer disabling long-term complications. The absence of effective therapies in ARDS, in general and in its COVID-19-associated form in particular, has triggered the search for therapies beyond classical pharmacological approaches. Since the start of the COVID-19 pandemic, it became clear that the major cellular inflammatory response elicited by organs affected with the virus also impacts their metabolic behavior [5]. Thus, achieving a positive cellular energy balance may result crucial for the recovery from COVID-19. We hypothesized that boosting two key pathways involved in cellular energy generation namely, AMP-activated protein kinase (AMPK)/acetyl-CoA carboxylase (ACC) signaling and fatty acid oxidation (FAO), could have a protective role in different experimental models mimicking COVID-19-associated inflammation and fibrosis in lung and kidney. To test this hypothesis, we used the drugs metformin (AMPK activator) and baicalin (CPT1A activator). While the knowledge about metformin is extensive and the clinical experience with its use is very broad [6], the FAO-enhancing flavonoid baicalin has not reached the clinical stage. Nevertheless, this is one of the few compounds with a selective capacity to enhance fatty acid oxidation (FAO) by virtue of its direct action on the FAO rate-limiting step catalyzed by carnitine palmitoyl transferases (CPTs), whose most abundant isoform in the lung and kidney is CPT1A [7]. We studied an animal model of ARDS, a cellular model (BEAS-2B cells) and a set of clinical data from patients with COVID-19 under previous treatment with metformin. Single-cell analysis of databases from patients affected with COVID-19 resulted useful in identifying cell populations from lung and kidney expressing a signature of metabolic derangement. We also explored the effects of metformin and baicalin in two animal models of kidney injury (folic acid nephropathy, FAN and unilateral ureteral obstruction, UUO) together with kidney epithelial cells (PTEC and HKC-8 cells) exposed to profibrotic mediators. We found that these energy metabolism enhancers were capable of inducing protection from inflammation and fibrosis in both lung and kidney in pathogenic settings, sharing important features with COVID-19.

Abbreviations

ARDS	acute respiratory distress syndrome
BAL	bronchoalveolar lavage
BMDMs	bone marrow-derived macrophages
CKD	chronic kidney disease
COVID-19	coronavirus disease 2019
ECM	extracellular matrix
EMT	epithelial-to-mesenchymal transition
FAO	fatty acid oxidation
FAN	folic acid nephropathy
FBS	fetal bovine serum
HRPTEC	human renal primary tubular epithelial cells
ITS	insulin-transferrin-selenium
OCR	oxygen consumption rate
SPF	specific pathogen free
TECs	tubular epithelial cells
T2DM	type 2 diabetes mellitus
UUO	unilateral ureteral obstruction

2. Results

2.1. Metformin and baicalin protect the lung from experimental ARDS

To test the effects of metformin and baicalin we used the LPS-induced experimental model of ARDS as shown in Fig. 1**A**. Treatment with each drug significantly protected from the establishment of fibrosis in the lung, as well as it markedly reduced the severity of ARDS-related pathological lesions and expression of fibrosis-associated genes (Fig. 1**B**, **C**, **D**, **E** and **H**). No synergistic beneficial effect of combined effect of Baicalin and Metformin was observed (data not shown). Increased levels of fibronectin were also observed in lungs from LPS-treated mice, whereas both metformin and baicalin drastically reduced this effect (Fig. 1**F** and **G**). While LPS was able to promote AMPK activation, this effect was not evident in the presence of metformin and baicalin (Fig. 1**F**). Evaluation of apoptosis in lung slices from the ARDS model by using BCL2 Associated X (BAX) immunohistochemistry showed that baicalin, but not metformin, abrogated LPS-induced cell death (Fig. 1**I** and **J**). In contrast, no effect of either drug was found on the increase of cell proliferation mediated by LPS (Supplemental Figs. 1A and B).

2.2. Metformin improves mitochondrial bioenergetics in human epithelial lung cells and inhibits TGF-β-induced profibrotic changes

To analyze the bioenergetic changes promoted by the tested compounds in a human setting, we established a cellular model of lung injury in BEAS-2B cells, which are of non-tumorigenic origin and share features with lung epithelial cells [8]. While metformin did not affect cell viability (Fig. 2**A**), it exerted a moderate suppressive effect of TGF-β-induced profibrotic, pro-inflammatory and pro-apoptotic gene expression profile by reducing the expression of genes inherent to epithelial-to-mesenchymal transition (EMT) (Fig. 2**B**). Noticeably, metformin increased palmitate oxidation in both the absence and presence of TGF-β and enhanced oxygen consumption rate (OCR), overcoming the inhibitory effect elicited by TGF-β (Fig. 2**C**–**E**). Treatment with TGF-β significantly increased fibronectin levels, an effect abrogated by metformin (Supplemental Figs. 2A and B). Interestingly, metformin did not modify TGF-β-induced SMAD3 phosphorylation (Fig. 2**F** and **G**) and was unable to revert TGF-β-induced increase in fibronectin levels when added 24 h after TGF-β (Fig. 2**H** and **I**). These results suggest that metformin is not affecting TGF-β signaling and hence, its beneficial effect is independent from this pathway. Most likely, it relies on AMPK activation [9]. To verify if p-AMPK activation by itself, excluding metformin off-target effects, could induce an antifibrotic effect, we tested the AMPK-activating compounds IND-6 and IND-8 [10] in the BEAS-2B model. We found that these compounds, especially IND-8, also offered protection against TGF-β-induced cellular injury and profibrotic effects (Supplemental Figs. 3A–H). Globally, these data support that triggering energy production by activating AMPK is a powerful approach towards protecting the lung from the highly deleterious changes associated to inflammation and fibrosis in the context of ARDS.

2.3. Baicalin improves mitochondrial bioenergetics in human epithelial lung cells and reverts TGF-β-induced p-SMAD3 phosphorylation and profibrotic changes

In the BEAS-2B cellular model, baicalin did not affect cell viability (Fig. 3**A**), whereas it exerted significant protection from TGF-β-induced increase in the expression levels of genes related to fibrosis, inflammation, apoptosis and EMT (Fig. 3**B**). Baicalin significantly prevented from TGF-β-induced increase in fibronectin protein levels, without modifying AMPK phosphorylation (Supplemental Figs. 2C and D). Similar to

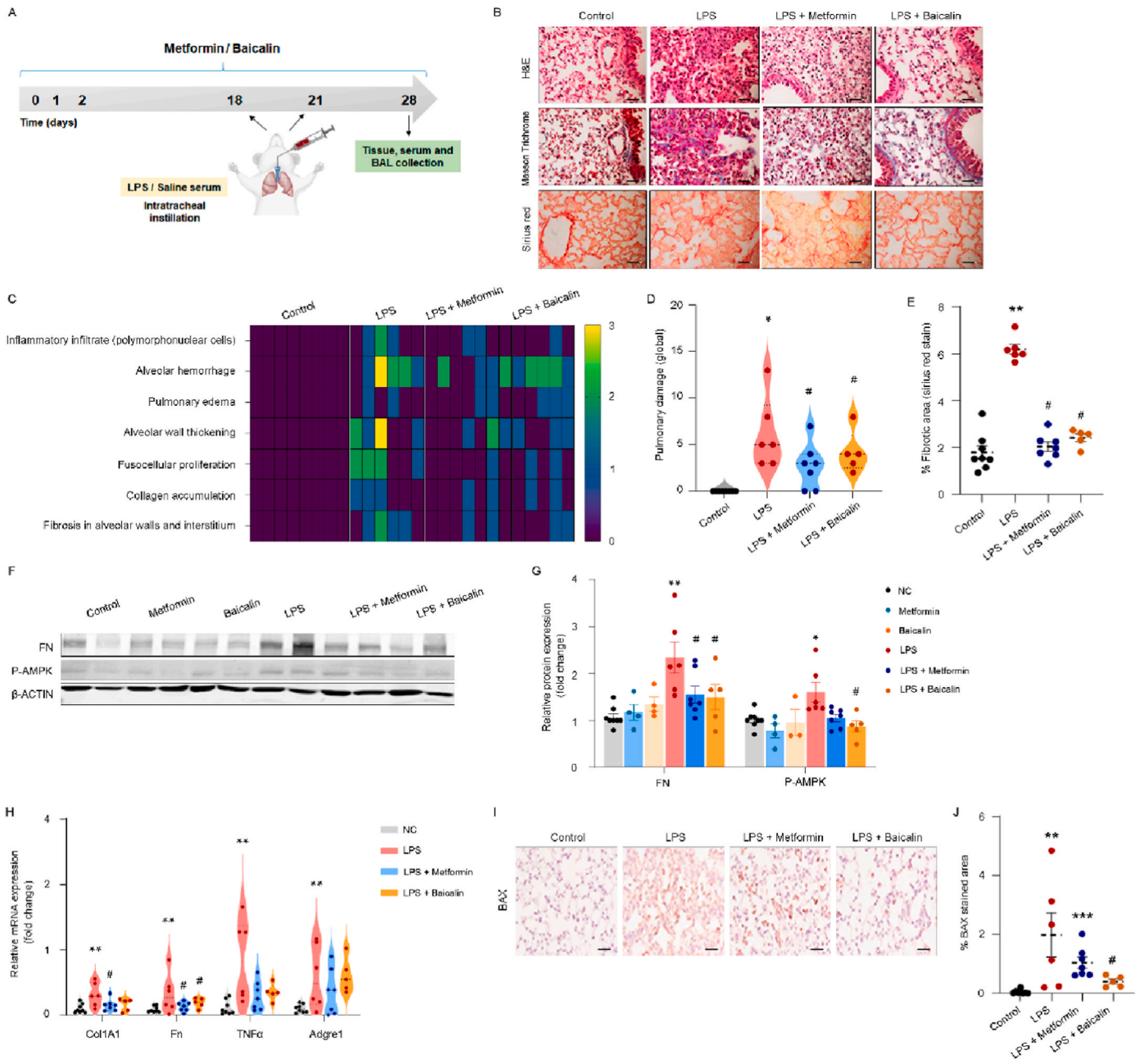

Fig. 1. Metformin and baicalin administration ameliorate lung damage and fibrosis in an animal model of LPS-induced ARDS. (A) Timeline of the LPS-induced ARDS mouse model and metformin/baicalin administration. **(B)** Representative microphotographs from one mouse per group of hematoxylin and eosin (H&E) (upper panels), Masson Trichrome (medium panels) and Sirius Red (lower panels) staining of lungs from mice subjected to LPS-induced ARDS after metformin/baicalin treatment. Scale bars: 25 μm. **(C)** Heat map of the anatomopathological study of the lung from mice treated as described above. **(D)** Violin plots of histological semi-quantitative global damage evaluation of the lungs from mice treated as described above. **(E)** Quantification of Sirius Red staining from (B) represents the mean ± s.e.m. **(F)** Immunoblots depicting fibronectin (FN), phosphorylated AMP-activated protein kinase (p-AMPK) protein levels in lungs from control and LPS-induced ARDS mice after metformin/baicalin treatment. **(G)** Bar graphs represent the mean ± s.e.m. of fold changes corresponding to densitometric analyses from (F), n = 6 mice. **(H)** Violin plots of mRNA levels of fibrosis-associated genes determined by qRT-PCR in lungs from mice treated as described above. Bar graphs represent the mean ± s.e.m. of fold changes. **(I)** Representative micrographs of one mouse per group showing the expression of BAX in lung sections of mice treated as described above. Scale bar = 25 μm. **(J)** Bar graph represents the quantification of the mean ± s.e.m. of % of BAX positive stained area in lungs from mice treated as described above. n = 5–8, mice *P < 0.05, **P < 0.01, ***P < 0.001 compared to control lungs; #P < 0.05 compared to lungs from LPS-induced ARDS mice. Statistical analysis for more than two groups was done with Kruskal-Wallis test. (For interpretation of the references to colour in this figure legend, the reader is referred to the Web version of this article.)

metformin, baicalin was able to promote increased palmitate oxidation and OCR, while preventing the inhibition of mitochondrial respiration induced by TGF-β (Fig. 3**C**–**E**). Of note, in contrast to metformin, baicalin did not activate AMPK, but was able to reduce TGF-β-induced SMAD3 phosphorylation and fibronectin protein levels when added simultaneously (Fig. 3**F** and **G**). In keeping, baicalin mitigated TGF-β-induced fibronectin accumulation when added after TGF-β (Fig. 3**H** and **I**). This data attest to a powerful antifibrotic effect of baicalin most likely occurring by the interference with TGF-β-signaling and direct activation of CPT1A.

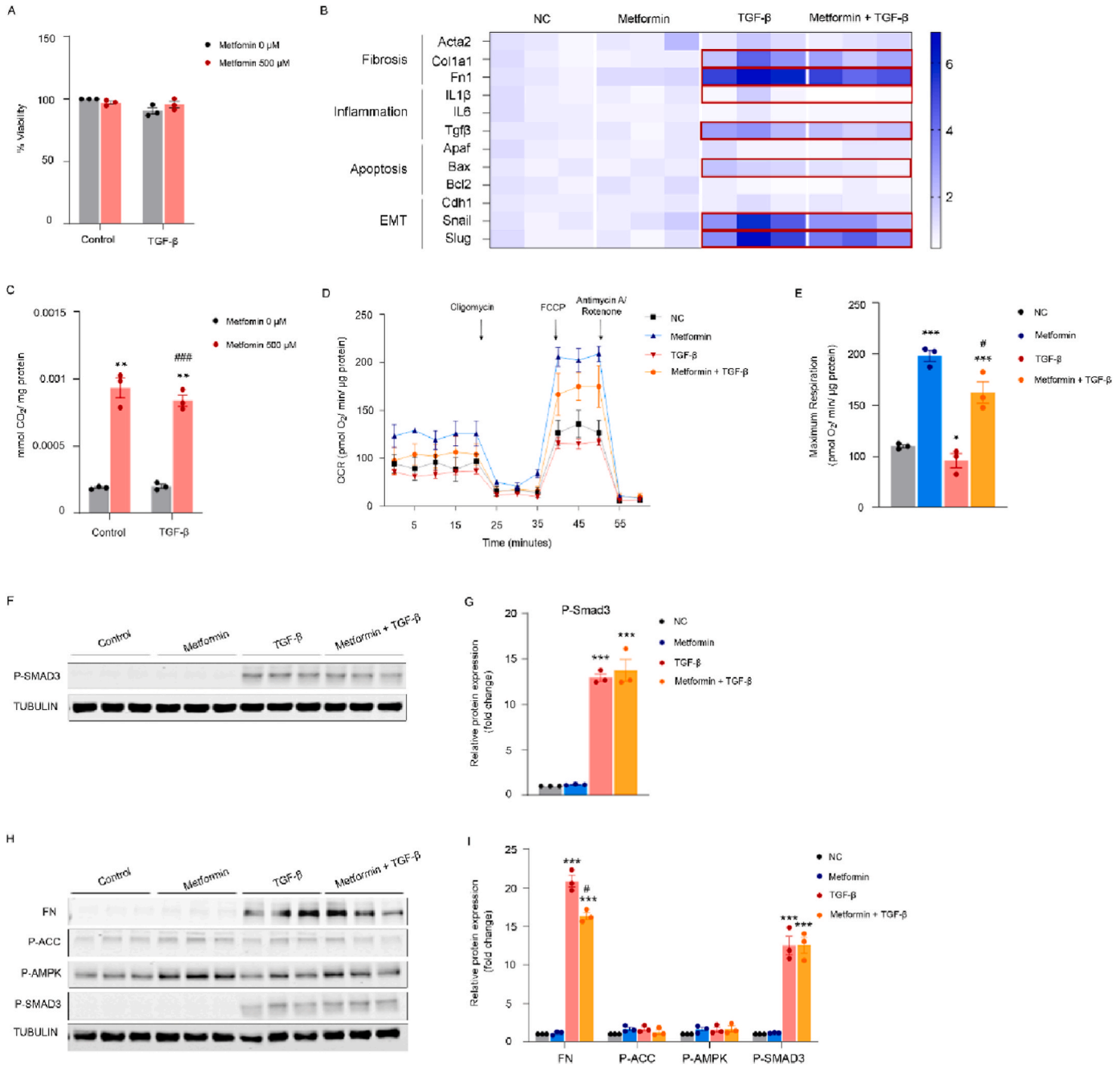

Fig. 2. Metformin increases mitochondrial function and decreases TGF-β-induced fibrosis, apoptosis and inflammation markers in human lung epithelial cells. (A) Bar graph represents the % of viable BEAS-2B cells under the treatment with 20 ng/ml TGF-β1 and/or 500 μM metformin. **(B)** Heat map of the mRNA levels of fibrosis-associated genes were determined by qRT-PCR in BEAS-2B cells treated as in (A). Genes whose expression is significantly reduced in the "Metformin + TGF-β1" condition compared to "TGF-β1" are boxed in red. **(C)** Radiolabeled palmitate-derived CO_2 was determined after incubation of cells treated as in (A) with ^{14}C-palmitate. **(D)** Oxygen consumption rate (OCR) of BEAS-2B cells treated as in (A) was measured with a Seahorse XFe96 Extracellular Flux Analyzer. **(E)** Bar graphs show the rates of OCR associated with maximum reserve capacity status. **(F)** Immunoblots depicting phosphorylated SMAD3 (p-SMAD3) protein levels in BEAS-2B cells treated with 20 ng/ml TGF-β1 and/or 500 μM metformin. **(G)** Bar graphs represent the mean ± s.e.m. of fold changes corresponding to densitometric analyses from (F). **(H)** Immunoblots depicting fibronectin (FN), phosphorylated AMP-activated protein kinase (p-AMPK), acetyl-CoA carboxylase (p-ACC) and SMAD3 (p-SMAD3) protein levels in BEAS-2B cells treated 500 μM metformin 24 h after than 20 ng/ml TGF-β1. **(I)** Bar graphs represent the mean ± s.e.m. of fold changes corresponding to densitometric analyses from (H). (A, B, C, F, H) n = 3 independent experiments. Each data point (D, E) represents the mean ± s.e.m of triplicate measures from 4 independent experiments. *P < 0.05, **P < 0.01, ***P < 0.001 compared to control cells; $^{\#}$P < 0.05, $^{\#\#\#}$P < 0.001 compared to cells treated with TGF-β1. Statistical analysis for more than two groups was done with Kruskal-Wallis test. (For interpretation of the references to colour in this figure legend, the reader is referred to the Web version of this article.)

2.4. Baicalin exhibits higher capacity than metformin to counteract macrophage-associated inflammation

In the initial phase of ARDS, resident alveolar macrophages (AM) sense the presence of microbial components (PAMPs such as LPS) or tissue injury (DAMPs such as HMGB1 and mitochondrial DNA) via the pattern recognition receptors (PRRs; e.g. TLR). PRR signaling leads to the NFκB-dependent polarization of AM into highly inflammatory M1

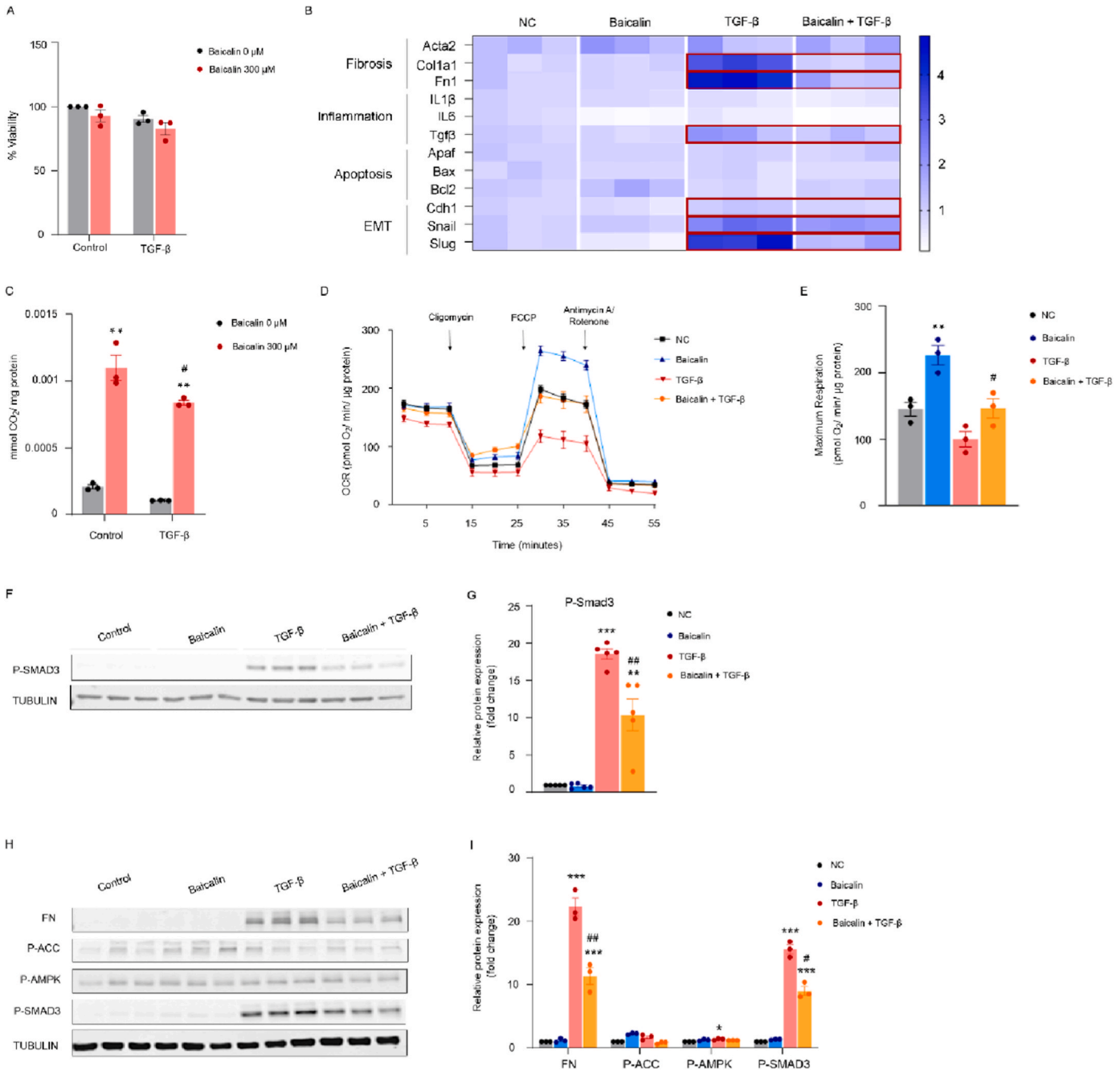

Fig. 3. Baicalin increases mitochondrial function and decreases TGF-β-induced fibrosis, apoptosis and inflammation markers in human lung epithelial cells. (A) Bar graph represents the % of viable BEAS-2B cells treated with 20 ng/ml TGF-β1 and/or 300 μM baicalin. **(B)** Heat map of the mRNA levels of fibrosis-associated genes were determined by qRT-PCR in BEAS-2B cells treated as in (A). Genes whose expression is significantly reduced in the "Baicalin + TGF-β1" condition compared to "TGF-β1" are boxed in red. **(C)** Radiolabeled palmitate-derived CO_2 was determined after incubation of cells treated as in (A) with ^{14}C-palmitate. **(D)** Oxygen consumption rate (OCR) of BEAS-2B cells treated as in (A) was measured with a Seahorse XFe96 Extracellular Flux Analyzer. **(E)** Bar graphs show the rates of OCR associated to maximum reserve capacity status. **(F)** Immunoblots depicting phosphorylated SMAD3 (p-SMAD3) protein levels in BEAS-2B cells treated with 20 ng/ml TGF-β1 and/or 300 μM baicalin. **(G)** Bar graphs represent the mean ± s.e.m. of fold changes corresponding to densitometric analyses from (F). **(H)** Immunoblots depicting fibronectin (FN), phosphorylated AMP-activated protein kinase (p-AMPK), acetyl-CoA carboxylase (p-ACC) and SMAD3 (p-SMAD3) protein levels in BEAS-2B cells treated 300 μM baicalin 24 h after than 20 ng/ml TGF-β1. **(I)** Bar graphs represent the mean ± s.e.m. of fold changes corresponding to densitometric analyses from (H). (A, B, C, F, H) n = 3 independent experiments. Each data point (D, E) represents the mean ± s.e.m of triplicates from 4 independent experiments. *P < 0.05, **P < 0.01, ***P < 0.001 compared to control cells; #P < 0.05, ##P < 0.01 compared to cells treated with TGF-β1. Statistical analysis for more than two groups was done with Kruskal-Wallis test. (For interpretation of the references to colour in this figure legend, the reader is referred to the Web version of this article.)

(or M1-like) macrophages and the initiation of the exudative phase [11]. In concordance, we found an increased abundance of the F4/80$^+$ total macrophage cell population, an effect that was markedly abrogated by baicalin (Fig. 4**A** and **B**). The presence of CD86$^+$ pro-inflammatory activated macrophages was also abrogated by the treatment with baicalin in murine lung tissue from the ARDS model (Fig. 4**A** and **C**). Consistently, the presence of IL-6, a major inflammatory cytokine related to COVID-19, was increased by LPS and significantly reduced by

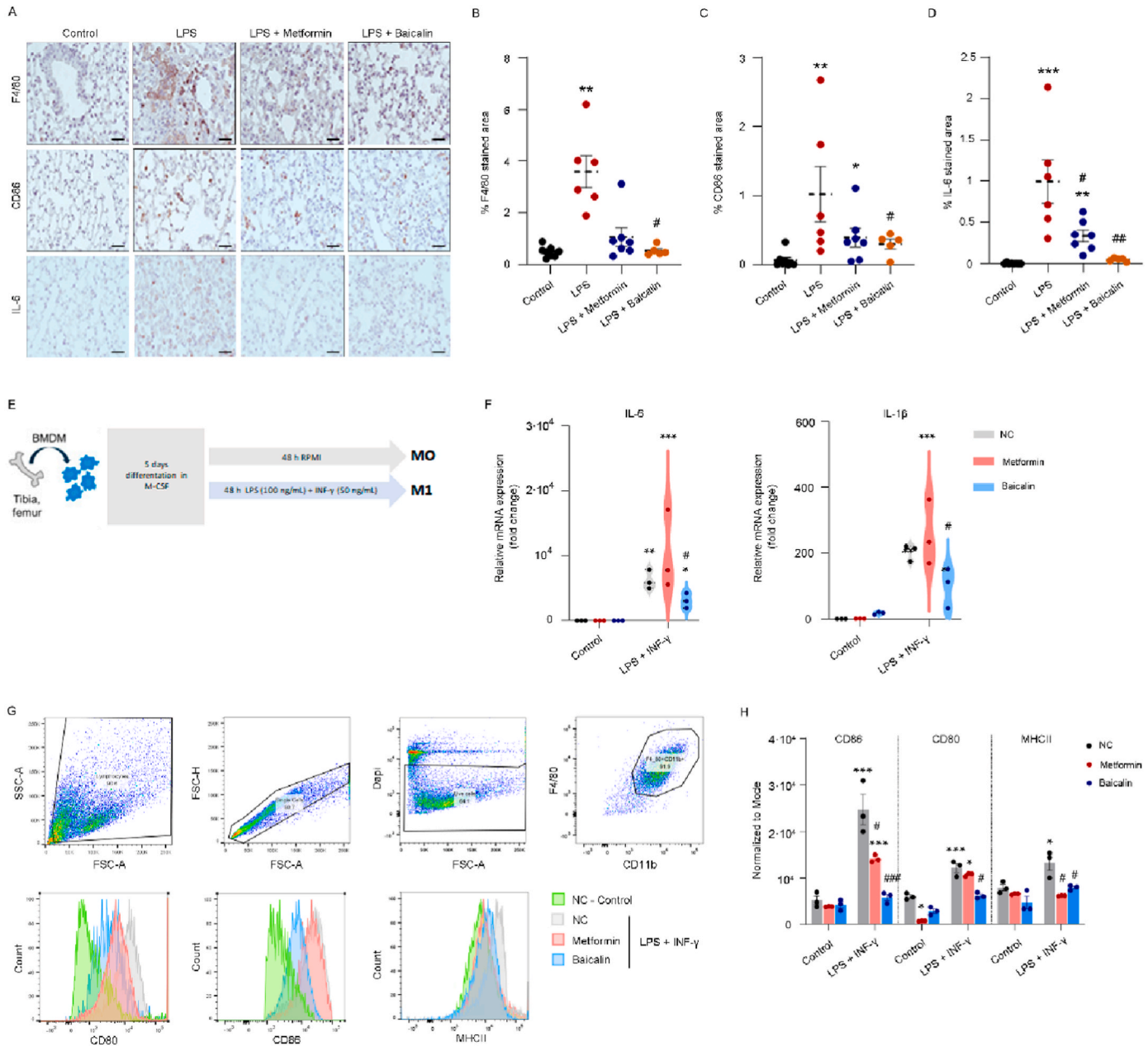

Fig. 4. Metformin and baicalin counteract macrophage-associated inflammation. (A) Representative micrographs of one mouse per group showing the expression of F4/80 (upper panels), CD86 (central panels) and IL-6 (lower panels) in lung sections of mice subjected to LPS-induced ARDS after Metformin/Baicalin treatment. Scale bar = 25 μm. **(B–D)** Bar graph represents the quantification of the mean ± s.e.m. of % of F4/80 (**B**), CD86 (**C**) and IL-6 (**D**) positive stained area in lungs from mice treated as described above. n = 5–8 mice. (**E**) Timeline of the bone marrow-derived macrophage (BMDM) differentiation toward an M1 macrophage phenotype. (**F**) mRNA levels of IL-6 and IL-1β were determined by qRT-PCR in BMDMs from (E) under 500 μM metformin or 300 μM baicalin treatment. (**G**) Representative multiparameter flow cytometry dot plots showing the gating strategy for BMDMs from (E) (upper panels). Fluorescence intensity distribution depicting the expression level of the macrophage activation markers: CD86, CD80 and MHCII determined by flow cytometry in the total BMDM population ($F4/80^{+}$, $CD11b^{+}$) under 500 μM metformin or 300 μM baicalin treatment (lower panels). (**H**) Bar graphs represent the fluorescence intensity of CD86, CD80 and MHCII from (G), median ± s.e.m of 3 independent experiments, each performed in triplicate. *P < 0.05, **P < 0.01, ***P < 0.001 compared to control lungs (B–D) or cells (F, H); $^{\#}$P < 0.05, $^{\#\#}$P < 0.01, $^{\#\#\#}$P < 0.001 compared to lungs from LPS-induced ARDS mice (B–D) or cells treated with LPS + INF-γ (F, H). Statistical analysis for more than two groups was done with Kruskal-Wallis test.

metformin or baicalin (Fig. 4**A** and **D**). We also tested the effects of these drugs on the activation of pro-inflammatory M1 murine bone marrow-derived macrophages (BMDMs) *in vitro* (Fig. 4**E**). We found that baicalin, but not metformin, prevented the expression of pro-inflammatory interleukins IL-6 and IL-1β in M1 BMDMs, while both metformin and baicalin prevented the BMDM differentiation toward an activated M1 macrophage phenotype (Fig. 4**F–H**). Overall, we found that both drugs significantly attenuated pro-inflammatory markers, albeit the effect of baicalin on the mitigation of macrophage-associated inflammation was more robust.

2.5. Previous treatment with metformin is associated with a less severe clinical presentation in patients with COVID-19

To validate our observations in experimental ARDS in the human setting, we first evaluated a cohort of 55 patients who had been

diagnosed with COVID-19 between March and June 2020, 15 of which had been on previous treatment with Metformin (Fig. 5**A**) (see Supplemental Table 1 for a complete description of the cohort). We found that the days of hospitalization and the proportion of patients who needed intensive care were reduced in the subset of patients who had been on previous treatment with Metformin (Fig. 5**B**), whereas no significant benefit was observed regarding respiratory modality treatment, dyspnea score during follow-up or other clinical parameters (Fig. 5**C** and **D**, Supplemental Fig. 4A and Supplemental Tables 2 and 3). A reduced expression of F4/80 was found in cells from in a limited number of bronchoalveolar lavage (BAL) samples from patients treated with metformin (Fig. 5**E**). However, the study of pro-inflammatory mediators in

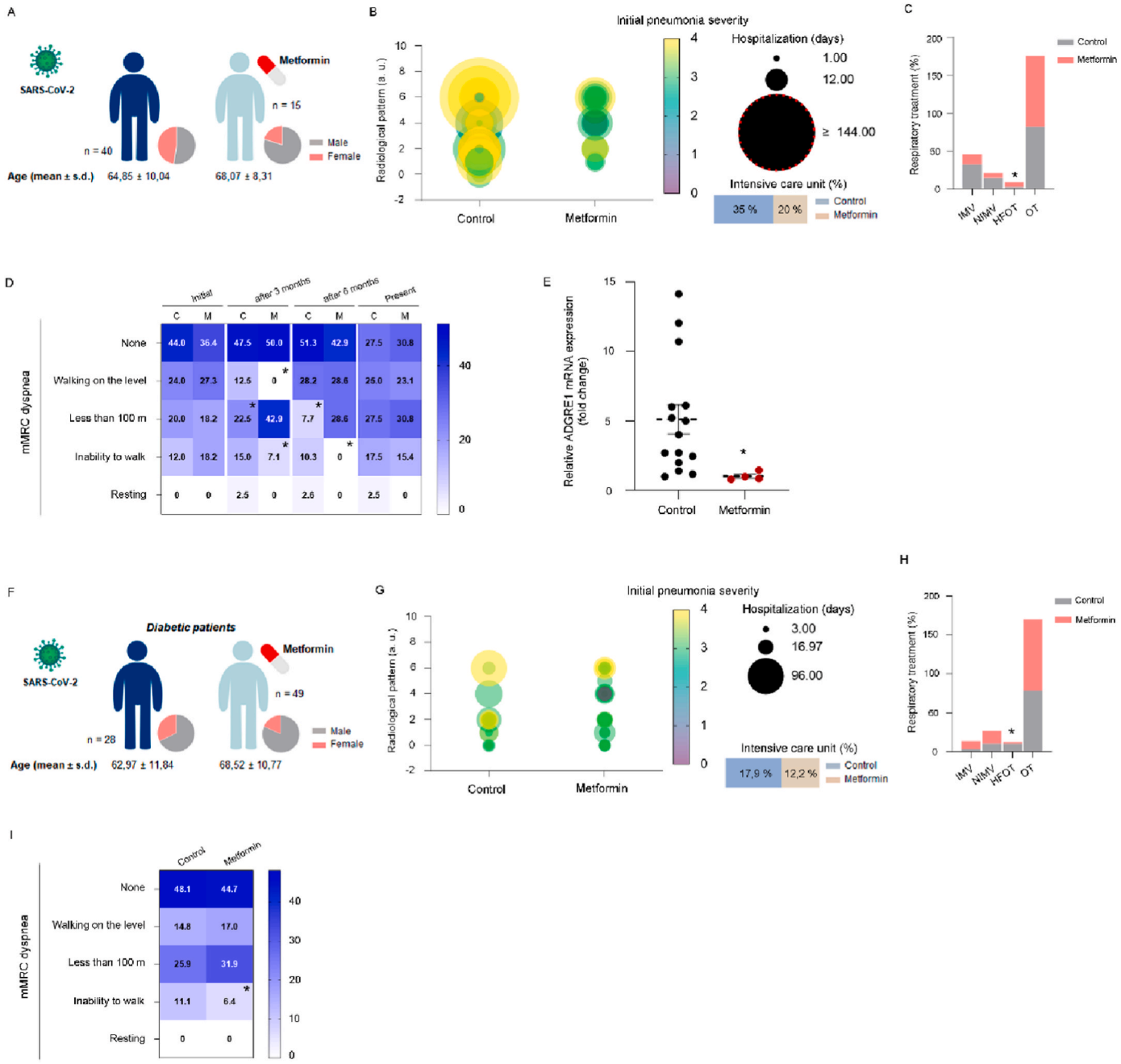

Fig. 5. Effect of metformin treatment on clinical parameters and outcomes in COVID-19 patients. (A) Graph depicting the characteristics (number of patients, age and sex) of the general patient cohort. **(B)** Bubble graph indicating initial pneumonia severity according to the radiological pattern (0: None, 1: Consolidation, 2: Ground-glass opacity, 3: Bronchiectasis, 4: Atelectasis, 5: Fibrosis, 6: Pulmonary embolism), days of hospitalization and % patients who needed intensive care within the cohort in (A). **(C)** Bar graph shows the % of different respiratory therapeutic modalities within patients from (A). IMV: Invasive mechanical ventilation, NIMV: Non-invasive mechanical ventilation, HFOT: High Flow Oxygen Therapy, OT: Oxygen therapy. **(D)** Heat map of the mMRC (modified Medical Research Council Dyspnea Scale) evaluation over time from patients in (A). **(E)** mRNA levels of ADGRE1 gene were determined by qRT-PCR in cells isolated from bronchoalveolar lavage (BAL) of 19 patients from cohort in (A). **(F)** Graph depicting the characteristics (number of patients, age and sex) of the diabetic patient cohort. **(G)** Bubble graph indicating initial pneumonia severity according to the radiological pattern, days of hospitalization and % patients who needed intensive care within the cohort in (F). **(H)** Bar graph shows the % of different respiratory therapeutic modalities as in (C) within patients from (F). **(I)** Heat map of the mMRC evaluation over time from patients in (F). *P < 0.05 compared to control. Statistical analysis for more than two independent groups was performed with Mann-Whitney test. The Chi-Square test was used to determine associations between variables.

such BAL samples from this cohort did not yield significant differences between patients treated or not with metformin (Supplemental Figs. 4B–D). We additionally evaluated another cohort of diabetic patients (n = 77), 49 of which were on chronic treatment with Metformin (Fig. 5**F** and Supplemental Table 4). In this cohort, we observed a less severe degree radiological pattern in the COVID-19-associated initial pneumonia and a slightly lower need of intensive care, with no added benefit in the rest of parameters evaluated (Fig. 5**G**–**I**, Supplemental Fig. 4E and Supplemental Table 5). We did not detect significant differences in co-morbidities related to autoimmune disorders or other inflammatory conditions aside from diabetes, affecting patients treated with or without metformin in any of the cohorts (Supplemental Figs. 4A and E). While these data do not allow to extract any definitive conclusion due to the retrospective nature of the study and the limited size of the cohorts, it is interesting to note the difference in the subsets of patients treated with Metformin regarding key features of the initial clinical presentation, such as severity of pneumonia or immediate need for intensive care.

Given the aforementioned limitations of our patient sample size and to gain insight into the potential role of the metabolic derangement occurring in alveolar epithelial cells (AT1 and AT2) associated with COVID-19, we analyzed the single-cell database available from a study with BAL samples from 10 COVID-19 patients (Supplemental Fig. 5A) [12]. As shown in Supplemental Figs. 5B and C, the expression levels of key genes related to mitochondrial metabolism, as well as the enrichment of citrate cycle and FAO routes was markedly depressed in infected AT1 and AT2 cells. Of interest, SARS-CoV-2 is present in COVID-19 patient kidney cells and induces fibrosis [13]. Similar trends regarding oxidative metabolism and fatty acid oxidation signatures were observed in renal epithelial cells (Supplemental Fig. 5D), attesting to the severe bioenergetics compromise associated to SARS-CoV2 infection.

2.6. *Metformin and baicalin protect against kidney injury and fibrosis in two different experimental models*

The kidney tubular epithelium is a compartment with a very high energetic demand due to its highly specialized transport and secretion functions. This energy is obtained from oxidative phosphorylation making tubular epithelial cells (TECs) highly vulnerable to hypoxia and inflammation. A reduction in FAO is a significant metabolic feature present in damaged TECs and both pharmacological and genetic strategies directed towards FAO enhancement have proven to be effective to protect from injury and fibrosis [14,15]. Hence, we tested the potential of metformin and baicalin to overcome the consequences of tubular injury in two well-known models of kidney injury, unilateral ureteral obstruction (UUO) (Fig. 6**A**) and folic acid-induced nephropathy (FAN) (Fig. 6**G**), which mimic some of the pathological derangements underlying fibrotic changes associated to chronic kidney disease (CKD). Both metformin and baicalin were able to significantly reduce the extent of fibrosis/inflammation promoted by UUO (Fig. 6**B**–**F**), while in the FAN model only baicalin was effective in preventing fibrosis-associated histological changes as well as collagen type I and fibronectin upregulation (Fig. 6**H-L**).

2.7. *Metformin and baicalin inhibit inflammation and fibrogenesis in human kidney epithelial cells while simultaneously enhancing FAO*

To validate our results in the human cellular setting, we studied the effects of metformin and baicalin in human renal primary tubular epithelial cells (HRPTEC) treated or not with the archetypal profibrotic cytokine TGF-β. None of these treatments resulted in decreased cellular viability (Fig. 7**A** and **F**). We found that both drugs suppressed the inflammatory and profibrotic gene expression profile elicited by TGF-β (Fig. 7**B**–**D** and **G-I**). Of importance, palmitate oxidation was depressed by TGF-β, an effect rescued only by Baicalin (Fig. 7**E** and **J**). Bioenergetics analysis in these cells showed that baicalin was more effective than metformin in preventing TGF-β-induced depression of OCR (Supplemental Figs. 6A–D).

These effects were also recapitulated in the human kidney cell line HKC-8, which also displayed a protective bioenergetics profile against TGF-β when treated with either Metformin or Baicalin (Supplemental Figs. 7 and 8). In consistence with our observations, in lung epithelial cells the AMPK-activating compounds IND-6 and IND-8 were also able to inhibit the profibrogenic effect of TGF-β in the HKC-8 cell line and, at the same time, counteract its depressive action on OCR (Supplemental Fig. 9). Taken together, these results expand the protective role of energy-enhancing drugs to the context of experimental kidney injury and human tubular epithelial cells.

2.8. *Increasing the genetic dose of tubular CPT1A correlates with enhanced protection from kidney fibrosis and inflammation*

Previous work from our laboratory demonstrated that conditional overexpression of CPT1A in the kidney tubule protected against fibrosis by improving FAO, bioenergetics and mitochondrial function [14]. Since those results had been obtained in heterozygous mice, we asked if homozygosity (Fig. 8**A** and **B**) would result in enhanced protection or, on the contrary, a deleterious effect. Homozygosity for the transgene responsible of CPT1A overexpression - Tg(tet(o)Cpt1a) - resulted in stronger enhanced renal CPT1A protein levels than in the case of heterozygosity (Fig. 8**C**–**E**). We did not find any increased lethality in Pax8-CPT1A mice after several weeks of breeding (data not shown) but, rather an increased level of protection after FAN, resulting in significantly lower fibrosis (Fig. 8**F**–**G**) and expression of profibrotic and inflammatory genes (Fig. 8**H**). Studies in epithelial cells derived from either heterozygous or homozygous transgenic mice overexpressing CPT1A (Supplemental Figs. 10A–D) corroborated the enhanced protection offered by an increased genetic dose regarding the anti-inflammatory response (Supplemental Fig. 10E) and the improved metabolic profile (Supplemental Fig. 10F).

3. Discussion

The pandemic caused by COVID-19 and the absence of specific antiviral therapies for SARS-CoV-2 necessarily triggered the interest in understanding the phases and mechanisms of human response to this infection. Hence, since the start of the pandemic, major advances in the biology of the virus and the immune response of infected hosts have taken place [16]. Because the immune response is intimately linked to changes in the metabolic status of cells, tissues and organs [5], attention was turned to identifying specific metabolic reprogramming within immune cell subpopulations. As a result, it was shown that patients affected by COVID-19 experience major metabolic alterations in most immune cell subpopulations, including T cells, B cells and monocytes, reflected in significant changes in the plasma metabolome and specific reprogramming in the gene expression profiles of each cell type [17]. These changes involve alterations in major metabolic pathways including glycolysis, lipid catabolism/synthesis and amino acid metabolism. In general, patients with COVID-19 experience a metabolic shift towards glycolysis, which may be detected in cells in charge of the innate and adaptive immune responses, as well as in epithelial cells of organs affected, such as the lung or kidney [18]. This adoption of a Warburg-type metabolic profile comes ultimately at the expense of a derangement in metabolic processes with higher capability of providing energy, such as fatty acid oxidation and oxidative phosphorylation, intimately linked to a preserved mitochondrial function. Indeed, mitochondrial dysfunction is a major pathogenic player in acute lung injury, including that related to COVID-19 [5,19], as well as in pulmonary fibrosis [20]. The rationale behind our study was to clarify if boosting mitochondrial provision of energy may contribute to the improvement of pathological responses in animal models related to COVID-19, as well as in patients affected with the disease. We found that activation of FAO

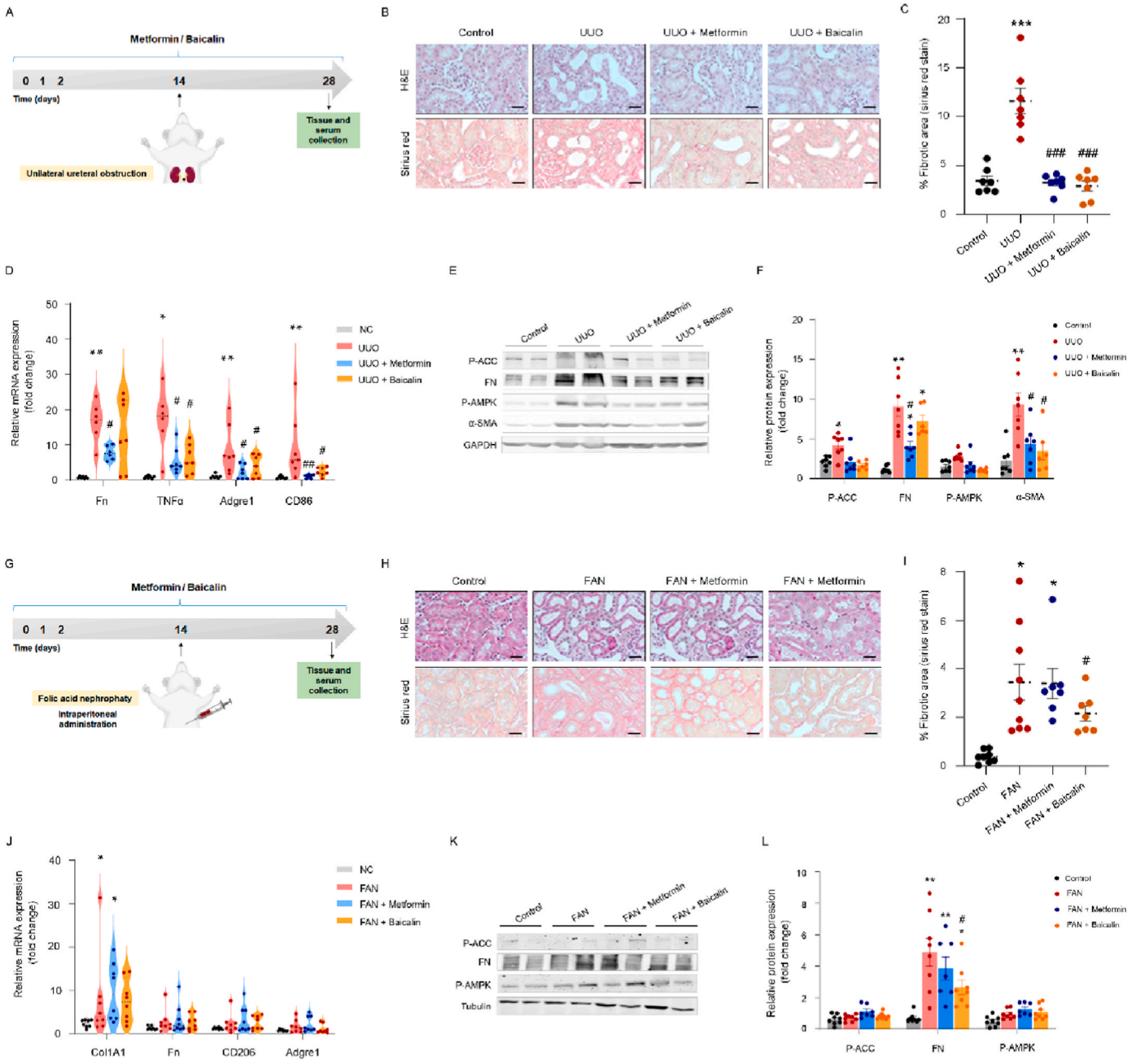

Fig. 6. Metformin and baicalin administration reduce UUO and FAN-induced kidney fibrosis. (A) Timeline of the unilateral ureteral obstruction (UUO) mouse model and metformin/baicalin administration. **(B)** Representative microphotographs from one mouse per group of hematoxylin and eosin (H&E) (upper panels) and Sirius Red (lower panels) staining of kidneys from mice subjected to UUO after metformin/baicalin treatment. Scale bars: 25 μm. **(C)** Quantification of Sirius Red staining from (B) represents the mean ± s.e.m, n = 7 mice. **(D)** Violin plots of mRNA levels of fibrosis-associated genes determined by qRT-PCR in kidneys from mice treated as described in (A). **(E)** Immunoblots depicting fibronectin (FN), phosphorylated AMP-activated protein kinase (p-AMPK) and alfa-smooth muscle actin (α-SMA) protein levels in kidneys from control and UUO mice after metformin/baicalin treatment. **(F)** Bar graphs represent the mean ± s.e.m. of fold changes corresponding to densitometric analyses from (E), n = 7 mice. **(G)** Timeline of the folic acid nephropathy (FAN) mouse model and metformin/baicalin administration. **(H)** Representative microphotographs from one mouse per group of hematoxylin and eosin (H&E) (upper panels) and Sirius Red (lower panels) staining of kidneys from mice subjected to FAN after metformin/baicalin treatment. Scale bars: 25 μm. **(I)** Quantification of Sirius Red staining from (H) represents the mean ± s.e.m, n = 6–10 mice. **(J)** Violin plots of mRNA levels of fibrosis-associated genes determined by qRT-PCR in kidneys from mice treated as described in (G). **(K)** Immunoblots depicting phosphorylated Acyl-CoA carboxylase (P-ACC), fibronectin (FN) and phosphorylated AMP-activated protein kinase (p-AMPK) protein levels in kidneys from control and FAN mice after metformin/baicalin treatment. **(L)** Bar graphs represent the mean ± s.e.m. of fold changes corresponding to densitometric analyses from (K), n = 7–9 mice. *P < 0.05, **P < 0.01, ***P < 0.001 compared to control lungs; #P < 0.05, ##P < 0.01, ###P < 0.001 compared to kidneys from mice subjected to UUO or FAN. Statistical analysis for more than two groups was performed with Kruskal-Wallis test. (For interpretation of the references to colour in this figure legend, the reader is referred to the Web version of this article.)

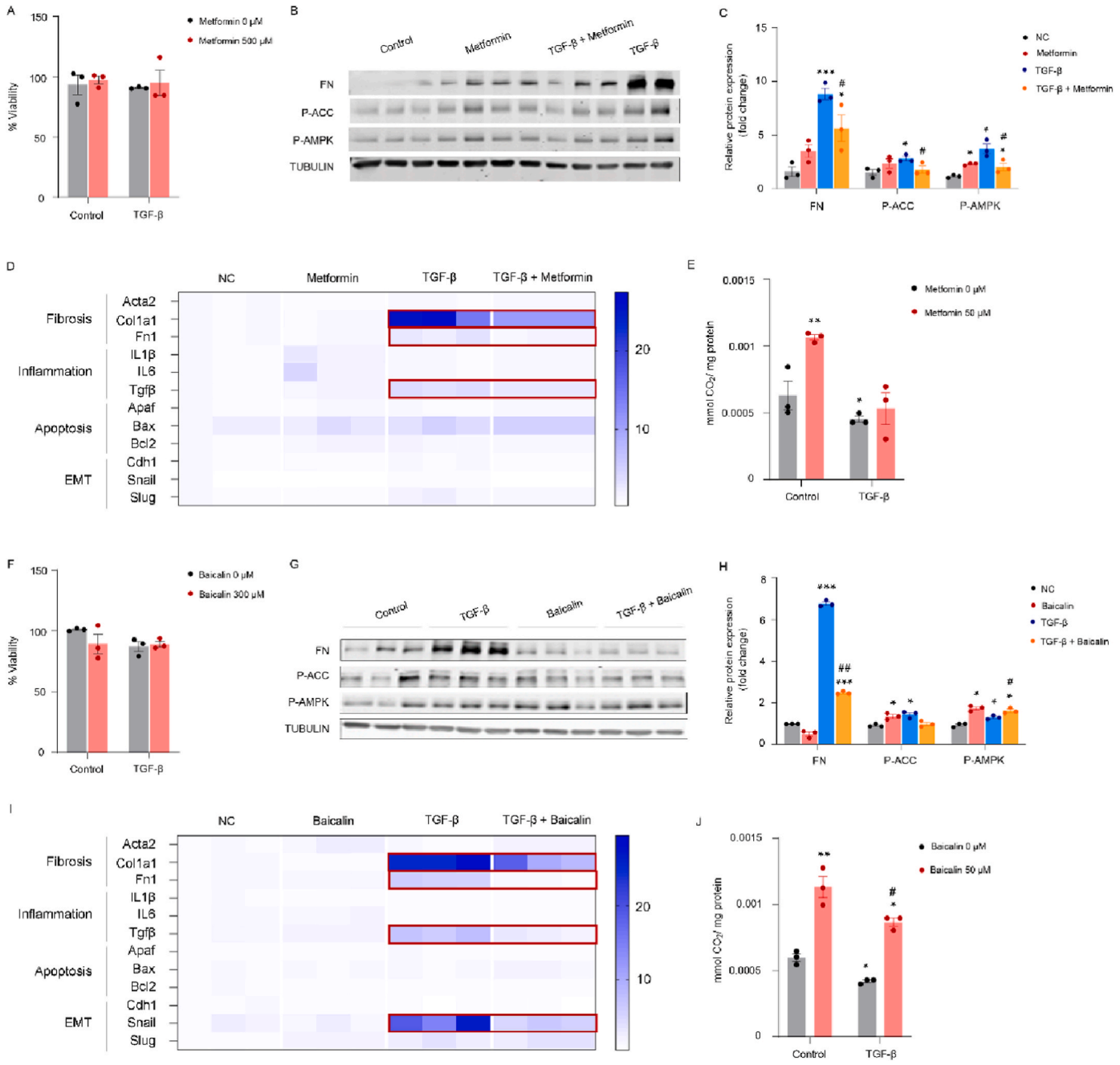

Fig. 7. Metformin and baicalin improve mitochondrial function and prevent TGF-β-induced renal epithelial cell dedifferentiation. (A) Bar graph represents the % of viable HRPTEC cells treated or not with 20 ng/ml TGF-β1 and/or 500 μM metformin. **(B)** Immunoblots depicting fibronectin (FN), phosphorylated AMP-activated protein kinase (p-AMPK) and acetyl-CoA carboxylase (p-ACC) protein levels in HRPTEC cells treated as in (A). **(C)** Bar graphs represent the mean ± s.e.m. of fold changes corresponding to densitometric analyses from (B). **(D)** Heat map of the mRNA levels of fibrosis-associated genes were determined by qRT-PCR in HRPTEC cells treated as in (A). Genes whose expression is significantly reduced in the "Metformin + TGF-β1" condition compared to "TGF-β1" are boxed in red. **(E)** Radiolabeled palmitate-derived CO_2 was determined after incubation of cells treated as in (A) with ^{14}C-palmitate. **(F)** Bar graph represents the % of viable HRPTEC cells treated or not with 20 ng/ml TGF-β1 and/or 300 μM baicalin. **(G)** Immunoblots depicting fibronectin (FN), phosphorylated AMP-activated protein kinase (p-AMPK) and acetyl-CoA carboxylase (p-ACC) protein levels in HRPTEC cells treated as in (F). **(H)** Bar graphs represent the mean ± s.e.m. of fold changes corresponding to densitometric analyses from (G). **(I)** Heat map of the mRNA levels of fibrosis-associated genes were determined by qRT-PCR in HRPTEC cells treated as in (F). Genes whose expression is significantly reduced in the "Baicalin + TGF-β1" condition compared to "TGF-β1" are boxed in red. **(J)** Radiolabeled palmitate-derived CO_2 was determined after incubation of cells treated as in (F) with ^{14}C-palmitate, n = 3 independent experiments. *P < 0.05, **P < 0.01, ***P < 0.01 compared to control cells; $^{\#}$P < 0.05, $^{\#\#}$P < 0.01 compared to cells treated with TGF-β1. Statistical analysis for more than two groups was done with Kruskal-Wallis test. (For interpretation of the references to colour in this figure legend, the reader is referred to the Web version of this article.)

through metformin or baicalin represent potential therapeutic strategies for COVID-19.

Metformin is a widely prescribed drug for the treatment of type 2 diabetes mellitus (T2DM) and has been also proposed as a senolytic [6, 21]. It has several mechanisms of action [22], even though one of the most importantly acknowledged biological effects is its capacity to activate the AMPK pathway, most likely through an indirect action, involving the inhibition of mitochondrial complex I [23] but also

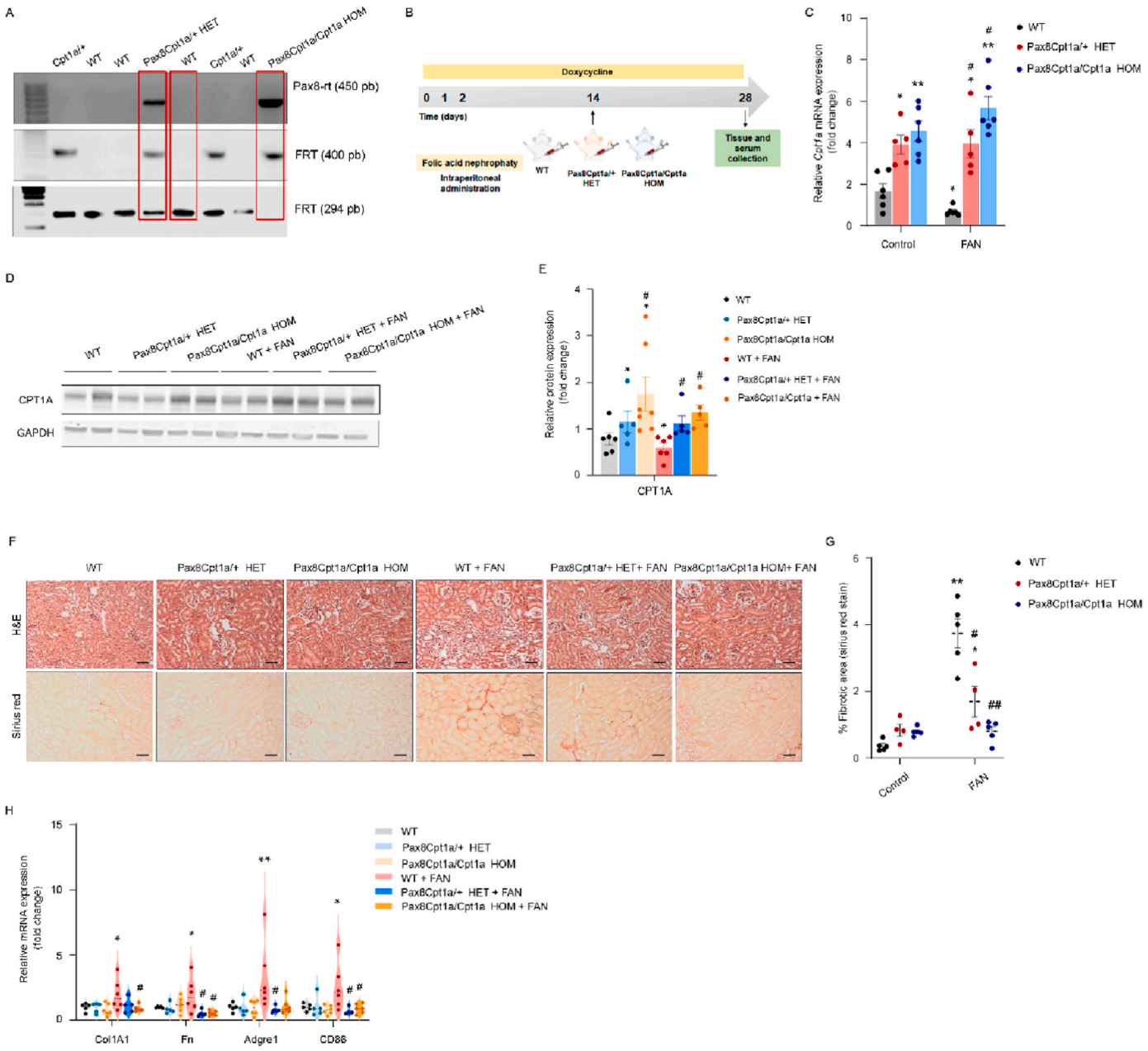

Fig. 8. Homozygous renal tubule overexpression of CPT1A results in enhanced protection from renal fibrosis. (A) Genomic DNA analysis by PCR for the Pax8-rtTA allele generates a 450-bp amplicon, while the FRT amplicons (400-bp and 294 bp) correspond to the tetO-Cpt1a alleles. The presence of two bands (left lane boxed in red) or a single 400-bp band (right lane boxed in red) denotes heterozygosity or homozygosity for the tetO-CPT1A allele, respectively. The 294-bp band (middle lane boxed in red) corresponds to the WT allele. See Supplemental Fig. 10A, Supplemental Table 6 and ref. [14] for details. **(B)** Timeline of the folic acid nephropathy (FAN) mouse model in control (WT), heterozygous (Pax8Cpt1a/+ HET) and homozygous (Pax8Cpt1a/Cpt1a HOM) CPT1A overexpressing mice. **(C)** mRNA levels of Cpt1a gene were determined by qRT-PCR in kidneys from mice treated as described in (B). **(D)** Immunoblots depicting CPT1A protein levels in kidneys from Pax8Cpt1a/+ HET or Pax8Cpt1a/Cpt1a HOM mice treated as described in (B). **(E)** Bar graphs represent the mean ± s.e.m. of fold changes corresponding to densitometric analyses from (D). **(F)** Representative microphotographs from one mouse per group of hematoxylin and eosin (H&E) (upper panels) and Sirius Red (lower panels) staining of kidneys from WT, Pax8Cpt1a/+ HET or Pax8Cpt1a/Cpt1a HOM mice subjected to FAN. Scale bars: 25 μm. **(G)** Quantification of Sirius Red staining from (F) represents the mean ± s.e.m. **(H)** Violin plots of mRNA levels of fibrosis-associated genes determined by qRT-PCR in kidneys from WT, Pax8Cpt1a/+ HET or Pax8Cpt1a/Cpt1a HOM mice treated as described in (B). Bar graphs represent the mean ± s.e.m. of fold changes, n = 6 mice. *P < 0.05, **P < 0.01 compared to control lungs; $^{\#}$P < 0.05, $^{\#\#}$P < 0.01 compared to kidneys from FAN mice. Statistical analysis for more than two groups was done with Kruskal-Wallis test. (For interpretation of the references to colour in this figure legend, the reader is referred to the Web version of this article.)

through binding PEN2, a subunit of γ-secretase [24]. Activation of AMPK is key for maintaining intracellular energy balance leading to increased catabolism and inhibition of anabolic pathways [25]. In the ARDS mouse model, closely related to COVID-19, we found that metformin reduced inflammation and fibrosis. We corroborated this protective action in human lung epithelial cells exposed to TGF-β, the major profibrotic cytokine, where metformin had a robust effect on AMPK activation. We had the opportunity of performing a retrospective analysis of two different patient cohorts (with and without T2DM), affected with COVID-19 lung disease, including a subset of patients in each cohort that had been chronically receiving metformin prior to their infection with SARS-CoV-2. In spite of the limitations of the cohort

design, our results are generally consistent with an improved clinical outcome, which is concordant with a meta-analysis involving a huge number of patients [26]. Importantly, since we initiated our study, accumulating evidence has mounted regarding the beneficial effects of metformin in COVID-19. Although definitive studies are still pending, a recent one evaluating the effect of metformin in the long term has shown that outpatient treatment with metformin significantly reduced long COVID incidence [27]. Similarly, a systematic review of randomized, placebo-controlled clinical trials of metformin treatment for acute COVID-19 showed improved clinical outcomes [28]. The most striking cellular finding in BAL samples from the patients to which we had access, was a reduction in the expression of the monocyte F4/80 marker (ADGRE1). This observation is also consistent with a potential benefit of metformin, likely by hampering the recruitment of myeloid cells to inflammatory foci, a hallmark of ARDS related to COVID-19 [12,29]. Metformin was also capable of reducing the pro-inflammatory profile in our experimental model of ARDS (Fig. 4), including the presence of key mediators in COVID-19 such as IL-6 [30,31]. Although we did not find significant changes in the few available BAL samples from patients that had been treated with metformin, mRNA levels of IL-6 tended to be lower (Supplemental Fig. 4C). The protection exerted by metformin against severe COVID-19 is certainly multifaceted [32]. However, pioneering studies in idiopathic pulmonary fibrosis point to a major, though not exclusive, role of AMPK [33,34]. Our results are fully in agreement with a strong metabolic, AMPK-dependent, effect of metformin as both in lung and kidney cellular models, it counteracted the profibrotic phenotype in close correlation to improved OCR and with biochemical evidence for AMPK activation. This is reinforced by data obtained with two indol-based compounds, which showed consistent protective effects and that have been shown to activate AMPK [10]. This activation is a major mechanism explaining the improvement of mitochondrial respiratory activity and has been suggested to promote increased FAO [35,36]. Our data regarding the effect of metformin on palmitate oxidation, in both lung and kidney epithelial cells, is concordant with this observation.

FAO is a key metabolic mitochondrial process supplying the cell with the appropriate energy output through the generation of acetyl-CoA and its entry into the TCA cycle. In recent years, it has been shown that a deficient energy balance related to FAO reduction plays a major pathogenetic role in lung and kidney injury [37–39]. Indeed, our group provided evidence by which FAO enhancement protects from kidney fibrosis in a genetically modified mouse model with heterozygous overexpression of CPT1A [14]. Of relevance and shown in this work, overexpression in homozygosity is even more protective against kidney fibrosis using the FAN model (Fig. 8**F–H**). We reasoned that baicalin, a flavonoid with the ability of directly binding and activating CPT1A [7] could represent a potential therapeutic molecule in the context of COVID-19. Our data show that in the murine ARDS, UUO and FAN models, as well as in lung and kidney epithelial cells under fibrogenic stimuli, baicalin is capable of preventing fibrosis along with a more favorable bioenergetics profile. Of interest, baicalin showed distinctive features from metformin regarding two important aspects. First, it was able to reduce the pro-inflammatory activated phenotype of BMDMs (Fig. 4E–H). Second, it succeeded in reverting TGF-β signaling-related changes and in reducing fibronectin levels even added after TGF-β (Fig. 3**H** and **I**). Thus, baicalin exerts an antifibrotic effect both by increasing FAO and, as previously reported and herein confirmed, by inhibiting TGF-β/Smad signaling pathway [40].

Moreover, single-cell analysis of databases from patients affected by pulmonary or renal COVID-19 disease showed reduced expression of mitochondrial genes key for oxidative phosphorylation and fatty acid metabolism. In keeping, decreased FAO and altered lactate production have been detected in the post-acute COVID-19 syndrome [41]. Further, extensive transcriptomics and metabolomics analyses in COVID-19 patients have evidenced accumulation of acyl-carnitines in full consistency with altered FAO and decreased CPT1A expression [42–44].

Our studies, performed in two different organs and using three experimental models, strongly support that in pathogenetic settings with high affinity to that posed by COVID-19, there is a critical deficit in energy in lung and kidney epithelia. This deficit relates to reduced FAO and the employment of two different drugs directed at improving mitochondrial bioenergetics prevents the development of inflammatory changes leading to organ fibrosis. Data from patients receiving metformin and single-cell analysis of lungs and kidneys from patients infected with COVID-19, support this tenet, also in the line of reports highlighting the importance of fatty acid metabolism in COVID-19 [45]. However, the current study presents some limitations. First, our experimental models did not directly test the response to COVID-19 infection, which could imply pathogenetic mechanisms different from the ones already provided by the models. Second, the study of the human cohort treated or not with metformin is retrospective and full confirmation of a beneficial effect of metformin would have required a double-blind, prospective, randomized clinical assay, a study which, to our knowledge, is not yet available. Regarding baicalin, there is lack of clinical studies as it has been proposed as potentially useful for COVID-19 only *in silico* and focusing on SARS-CoV-2 proteases [46]. Although our data provide experimental evidence for its antifibrotic action in two different organs, lung and kidney, and in direct relation with its capacity to increase FAO, the experimental design of this study does not allow to infer definitive conclusions about the curative potential of either metformin or baicalin, since both of them were administered prior to the injury phase. Notwithstanding, we believe that this and other future studies may contribute to foster research directed at specific therapeutic approaches involving FAO enhancement within epithelial cell subpopulations, which are undoubtedly the critical targets of COVID-19 infection and whose function ultimately compromises organ survival.

4. Materials and Methods

4.1. Cell lines and culture conditions

Immortalized human bronchial epithelial cells BEAS-2B obtained from the American Type Culture Collection Collection (ATCC®; #CRL-9609) were cultured in BEBM (Bronchial Epithelial Cell Growth Basal Medium) supplemented with SingleQuot kit additives (Lonza, Walkersville, MD). Human proximal tubular epithelial cells (HKC-8) (kindly provided by Dr. Kathalin Susztak) were cultured in DMEM/F12 (Dulbecco's modified Eagle's medium 1:1 (v/v)) (Corning, New York, NY) supplemented with 15 mM Hepes, 5% (vol/vol) fetal bovine serum (FBS) (HyClone Laboratories, Logan, UT), 1x Insulin-Transferrin-Selenium (ITS) (Gibco, Rockville, MD), 0.5 μg/ml hydrocortisone (Sigma-Aldrich, St. Louis, MO), 50 units/mL penicillin and 50 μg/mL streptomycin (Gibco, Rockville, MD). Immortalized renal human proximal tubule epithelial cells RPTEC/TERT1 (HPTEC) (ATCC®; #CRL-4031) were cultured in DMEM/F12, GlutaMAX supplement (Dulbecco's modified Eagle's medium 1:1 (v/v)) (Life technologies, MA, USA) supplemented with 20 mM Hepes, 2% (v/v) fetal bovine serum (FBS) (HyClone Laboratories, Logan, UT), 5 μg/ml Apo-transferrin (Sigma-Aldrich, St. Louis, MO), 5 μg/ml Human Insulin Solution (Sigma-Aldrich, St. Louis, MO), 50 nM dexamethasone (Sigma-Aldrich, St. Louis, MO), 3 nM 3,3′,5-Triiodo-L-thyronine sodium salt (Sigma-Aldrich, St. Louis, MO), 10 ng/ml EGF (Sigma-Aldrich, St. Louis, MO), 60 nM Selenium (Sigma-Aldrich, St. Louis, MO), 50 units/ml penicillin and 50 μg/ml streptomycin (Gibco, Rockville, MD, USA). All cells were cultured at 37 °C and 5% CO_2 and treated with trypsin every five days for sub-culturing. In the case of BEAS-2B cells, plates were coated with 0.01 mg/ml human fibronectin (ThermoFisher Scientific, Waltham, MA), 0.03 mg/ml bovine collagen type I (Advanced BioMatrix, San Diego, CA) and 0.01 mg/ml bovine serum albumin (BSA) in BEBM basal medium for at least 2 h at 37 °C prior to plating. Treatments with human recombinant 20 ng/ml TGF-β1 (R&D Systems, Minneapolis, MN) and drug treatments: 500 μM Metformin, 300 μM Baicalin (both from Sigma-Aldrich, St.

Louis, MO) and 50 μM indols (IND6 and IND8) were performed for 24 h (h) after 12 h of serum-free starvation for subsequent mRNA and protein expression analysis.

4.2. Isolation of primary kidney epithelial cells

Kidneys from 3- to 5-week-old CPT1A KI male mice were collected after sacrifice and minced into pieces of approximately 1 mm^3. These pieces were digested with 10 ml HBSS containing 2 mg/mL collagenase I (Thermo Scientific, Rockford, IL) for 30 min at 37 °C with gentle stirring and supernatants were sieved through a 100-μm nylon mesh. After centrifugation for 10 min at 3000 rpm, the pellet was resuspended in sterile red blood cell lysis buffer (8.26 g NH4Cl, 1 g KHCO3, and 0.037 g EDTA per 1 L ddH2O) and seeded in 10-cm culture dishes. Cells were cultured in RPMI 1640 (Corning, New York, NY) supplemented with 10% FBS (HyClone Laboratories, Logan, UT), 20 ng/mL EGF (Sigma-Aldrich, St. Louis, MO), 20 ng/ml bFGF (Sigma-Aldrich, St. Louis, MO), 50 units/mL penicillin and 50 μg/mL streptomycin (Gibco, Rockville, MD) at 37 °C and 5% CO_2. Cells were used between days 7 and 10 of culture. GFP was assessed by using an inverted microscope Axiovert200 coupled to a monochrome sCMOS camera with a 20X/0.5 Plan-Neofluar objective (Zeiss, Oberkochen, Germany).

4.3. Mouse models of lung and kidney injury

Mice were housed in the Specific-pathogen-free (SPF) animal facility at the Centro de Biología Molecular Severo Ochoa (CBMSO) in accordance with EU regulations for all the procedures. Animals were handled in agreement with the Guide for the Care and Use of Laboratory Animals contained in Directive 2010/63/EU of the European Parliament. Approval was granted by the local ethics review board of the CBMSO in Madrid, the Ethics committee at CSIC and the Regulatory Unit for Animal Experimental Procedures from the Comunidad de Madrid. Mice were of the strain C57BL/6J obtained from Charles River laboratories and were housed in colony cages with a 12:12-h light-dark cycle in a temperature- and humidity-controlled environment with free access to water. Metformin (Sigma-Aldrich, St. Louis, MO) was administered to mice at 1,5 mg/mL dissolved in drinking water for 28 days, while baicalin (Sigma-Aldrich, St. Louis, MO) was administered daily to mice at 500 mg/kg body weight in 0.5% carboxymethyl cellulose (CMC) (Wako Pure Chemical Industries Ltd., Osaka, Japan) by oral gavage for 28 days. Control animals received daily 0.5% CMC administered by oral gavage for the same period of time. Lung and kidney mouse models were carried out 14 days after initiation of metformin/baicalin administration which was maintained until mice sacrifice. At this time point, plasma concentration of metformin was 3.81 μM, while in the case of Baicalin it was under the HPLC detection limit (data not shown). LPS-induced acute respiratory distress syndrome (ARDS) was performed by intratracheal (i.t) instillation of lipopolysaccharide (LPS), as previously described [47,48]. LPS 055:B5 (Sigma-Aldrich, St. Louis, MO) was administered twice with a (three-day spaced dosing) at a concentration of 5 mg/kg weight, dissolved in saline serum and delivered in a volume of 2 μL/g of weight. Control animals received 0.05 ml of vehicle (i.t). Unilateral ureteral obstruction (UUO) surgery procedure was performed as previously described [49]. Briefly, 12–14 weeks old mice were anesthetized with 2% isoflurane. The hair in the abdominal area was shaved. An incision was made in the abdominal wall to expose the left kidney, the ureter was ligated twice and severed between the two ligatures and the kidney was returned gently to its anatomical position. Finally, the abdominal incision was closed with sutures and buprenorphine was used as an analgesic. Folic acid-induced nephropathy (FAN) was induced by intraperitoneal (i.p) injection with 250 mg folic acid (Sigma-Aldrich, St. Louis, MO) per kg body weight dissolved in 0.3 M sodium bicarbonate (vehicle) as previously described [50]. Control animals received 0.3 ml of vehicle (i.p). Mice were sacrificed by CO_2 overdose and lung and blood samples were harvested after perfusion with PBS after 10 day of the first LPS instillation. Kidney and blood samples were collected following the same procedure after 15 days of UUO or FA administration.

4.4. Doxycycline induction

To induce CPT1A expression, 8-week-old Tg(Pax8-rtTA)/+; Tg(tet(o)Cpt1a)/Tg(tet(o)Cpt1a) (summarized as Pax8Cpt1a/Cpt1a HOM), Tg(Pax8-rtTA)/+; Tg(tet(o)Cpt1a)/+ (summarized as Pax8Cpt1a/+ HET) mice and corresponding WT mice (Tg(tet(o)Cpt1a)/+ were used as control mice) were fed with doxycycline (Sigma-Aldrich, St. Louis, MO) at concentrations of 1 mg/ml via drinking water for 4 weeks. In the FAN model, doxycycline administration starts 15 days after FA injection.

4.5. Genotyping

CPT1A KI mice were genotyped by PCR using DNA extracted from tail biopsies and the primers listed in Supplemental Table 6. DNA extraction was performed by using the AccuStart™ II Mouse Genotyping Kit according to the manufacturer's instructions.

4.6. Isolation and polarization of murine bone marrow-derived macrophages and characterization of populations by flow cytometry

Murine BMDMs were isolated as previously reported [51]. Briefly, bone marrow was flushed from fresh femurs and tibiae of 8- to 10-week-old C57BL/6J mice after CO_2 euthanasia. Single-cell bone marrow cell suspension was cultured at a density of 10^6 cells/mL in RPMI-1640 medium (Invitrogen, Carlsbads, CA) containing 10% (vol/vol) FBS (Gibco, Rockville, MD), 50 nM β-mercaptoethanol, 2 mM L-glutamine (HyClone Laboratories, Logan, UT), 100 U/mL penicillin (Sigma-Aldrich, St. Louis, MO), 100 μg/mL streptomycin (Sigma-Aldrich, St. Louis, MO), non-essential amino acids (HyClone Laboratories, Logan, UT), 1 mM sodium pyruvate (HyClone Laboratories, Logan, UT), 10 mM HEPES (Hyclone, UT, USA) and 50 μM β-mercaptoethanol (Sigma-Aldrich, St. Louis, MO) and 30% (vol/vol) M-CSF containing supernatant from L929 cell line at 37 °C under 5% CO_2. Bone marrow macrophage medium was refreshed on day 3 and mature M0-macrophages were generated on day 7. M1-polarization was induced by 100 ng/mL LPS from *Escherichia coli* (EK; Invivogen, San Diego, CA) and 50 ng/mL recombinant murine IFN-γ (PeproTech, London, UK) overnight. Characterization of murine bone marrow-derived macrophage polarization was assessed by multiparametric flow cytometry using corresponding antibodies listed in Supplemental Table 7. Purified anti-FcγRIII/II (2.4G2, TONBO Bioscience) was used to block murine Fc-receptors. Fluorescence intensity was measured in a LSRFortessa (BD Biosciences, Eysins, Switzerland) and analyzed with FlowJo 10.9 software. Cell gating was initially based in the forward versus side scatter (FSC vs. SSC) plot. Next, dead cells were excluded by Dapi (1:5000, Sigma-Aldrich, St. Louis, MO). Identification of the macrophage cell population was based on the presence of F4/80 and Cd11b. Numbers in quadrants indicate cell proportions. Activated macrophages exhibit elevated levels of costimulatory and antigen-presenting molecules, such as CD80, CD86 and MHC class II molecules. Their expression was displayed as a histogram and their median of fluorescence intensity was obtained. For each sample, at least 20,000 singlets were analyzed in triplicates.

4.7. Immunoblot

Cells or a quarter piece of each kidney sample were homogenized and lysed in 100/300 μL RIPA lysis buffer containing 150 mM NaCl, 0.1% SDS, 1% sodium deoxycholate, 1% NP-40 and 25 mM Tris–HCl pH 7.6, in the presence of protease (Complete, Roche Diagnostics, Mannheim, Germany) and phosphatase inhibitors (Sigma-Aldrich, St. Louis, MO). Samples were clarified by centrifugation at 10,000 g for 15 min at 4 °C. Protein concentrations were determined by the BCA Protein Assay

Kit (Thermo Scientific, Rockford, IL) and was measured in Glomax®-Multi Detection system (Promega, Madison, WI). Equal amounts of protein (10–50 μg) from the total extract were separated on 8–10% SDS–polyacrylamide gels and transferred onto nitrocellulose blotting membranes (GE Healthcare, Chicago, IL) at 12 V for 20 min in a semi-dry Trans-Blot Turbo system (Bio-Rad, Hercules, California). Membranes were blocked by incubation for 1 h with 5% non-fat milk in PBS containing 0.5% Tween-20 and blotted overnight with the specific antibodies listed in Supplemental Table 8. After incubation with IRDye 800 goat anti-rabbit and IRDye 600 goat anti-mouse (1:15,000, LI-COR Biosciences, Lincoln, NE) secondary antibodies, membranes were imaged with the Odyssey Infrared Imaging System (LI-COR Biosciences, Lincoln, NE). Band densitometry was performed using the ImageJ 1.48 software (http://rsb.info.nih.gov/ij) and relative protein expression was determined by normalizing to β-actin or tubulin. Fold changes were normalized to values of control condition.

4.8. RNA extraction

Total RNA was extracted from cell lines, mouse kidneys or BAL using the RNeasy Mini Kit (Qiagen, Valencia, CA) according to the manufacturer's instructions. In the case of BAL, samples were previously centrifuged at 3000 rpm for 10 min and RNA was extracted from the pellet. RNA quantity and quality were determined at 260 nm by a Nanodrop-1000 spectrophotometer (Thermo Scientific, Rockford, IL).

4.9. Analysis of mRNA expression

Reverse transcription (RT) was carried out with 500 ng of total RNA using the iScript™ cDNA Synthesis kit (Bio-Rad, Hercules, CA). qRT–PCR was carried out with the iQ™SYBR Green Supermix (Bio-Rad, Hercules, CA), using a 96-well Bio-Rad CFX96 RT–PCR System with a C1000 Thermal Cycler (Bio-Rad, Hercules, CA) according to the manufacturers' instructions. A C_t value was obtained from each amplification curve using CFX96 analysis software provided by the manufacturer. Relative mRNA expression was determined using the $2^{-\Delta\Delta Ct}$ method [52]. The 18S gene was used for normalization purposes. The primer sequences used for mRNA quantification are listed in Supplemental Table 9. Fold changes were normalized to values of control condition.

4.10. [1–14C] palmitate oxidation

Measurement of fatty acid oxidation (FAO) rates was performed in cells as previously described [53]. Briefly, cells were seeded in 12-well dishes to reach a confluence of 70% and treated with the corresponding drugs as described in the cell lines and culture conditions procedure section. Then, cells were incubated in 500 μL of media containing 0.3% BSA/100 μM palmitate/0.4 μCi/mL ^{14}C-palmitate at 37 °C for 3 h. Each sample was assayed in triplicate. The reaction was stopped by the addition of 200 μl of 1 M perchloric acid. The rate of palmitate oxidation was measured as released $^{14}CO_2$ trapped in a filter paper disk with 20 μL of 1 M NaOH in the top of sealed vials. ^{14}C products were counted in an LS6500 liquid scintillation counter (Beckman Instruments Inc., Brea, CA). Scintillation values were converted to mmol $^{14}CO_2$ multiplying by the specific activity and normalized to the protein content.

4.11. Measurements of oxygen consumption rate

Oxygen consumption rate (OCR) (ligated to oxidative phosphorylation) was studied using the Seahorse Bioscience metabolic analyzer for the Cell Mito Stress Test, the Palmitate Oxidation Stress Test and the Real-Time ATP Rate Assay, according to the manufacturer's instructions [54]. Cells were firstly seeded in a p60 plate and when they reached a confluence of 70% they were treated with the corresponding drugs as described in the cell lines and culture conditions procedure section. In the case of BEAS-2B or HKC-8 cells, OCR was determined by using the Cell Mito Stress Test. Cells were seeded at 2×10^4 cells per well in a Seahorse Bioscience XFe96 cell culture microplate (Seahorse Bioscience, North Billerica, MA). One hour before the assay measurement, growth medium was replaced with substrate-limited medium, Dulbecco's Modified Eagle Medium (DMEM) supplemented with 0.5 mM Glucose and 1 mM Glutamate and cells were incubated for 1 h at 37 °C without CO_2. Immediately, XF Cell Mito Stress Test was performed in a Seahorse XFe96 energy analyzer by sequentially adding several modulators of mitochondrial function: 1 μM oligomycin (Sigma-Aldrich, St. Louis, MO), 3 μM cyanide 4-(trifluoromethoxy) phenylhydrazone (FCCP) (Sigma-Aldrich, St. Louis, MO) and 1 μM antimycin/rotenone (Sigma-Aldrich, St. Louis, MO). Values were normalized for total protein content. Basal mitochondrial respiration, ATP-linked respiration, proton leak (non-ATP–linked oxygen consumption), maximal respiration, non-mitochondrial respiration and reserve respiratory capacity were determined as described [55]. In the case of HPTECs, OCR was determined by using the Palmitate Oxidation Stress Test. Cells were seeded at $3x10^4$ cells per well. One hour before the assay measurement, medium was replaced with substrate-limited medium: DMEM supplemented with 2 mM Glucose and 0.5 mM L-Carnitine and cells were incubated for 1 h at 37 °C without CO_2. 200 μM palmitate-BSA was added just prior to starting the assay. Immediately, XF Palmitate Oxidation Stress Test was performed by adding 1.5 μM oligomycin, 2 μM FCCP and 0.5 μM antimycin/rotenone. In the case of primary kidney epithelial cells, ATP production rates were determined by using the Real-Time ATP Rate Assay. Cells were seeded at 10^4 cells per well. The injection of 1 μM oligomycin and 1 μM antimycin/rotenone enabled the calculation of mitochondrial and glycolytic ATP production by using Agilent ATP Assay Report Generator. Four wells were used for each experimental group. Values were normalized for protein content or cell number.

4.12. Histological analysis

A quarter piece of each lung/kidney sample was immersed in 4% neutral buffered formalin for 24 h, embedded in paraffin, cut in serial sections (5 μm thickness) and stained with hematoxylin and eosin (H&E), Sirius red and Masson's Trichrome as described previously [56]. Fibrosis was quantified in Sirius red-stained sections in order to detect collagen fibers. The area of interstitial fibrosis was identified, after excluding the vessel area from the region of interest, as the ratio of interstitial fibrosis or collagen deposition to total tissue area and expressed as %FA (fibrotic area). For each tissue, 10–15 fields were analyzed with a 40X objective lens under transmitted light microscopy by using a digital camera (Nikon D3) connected to a Nikon's Eclipse TE2000-U light microscope (Nikon Instruments Europe B.V., Badhoevedorp, The Netherlands). Intensity measurements of Sirius red staining area were performed blindly in an automated mode using the ImageJ 1.48 software (http://rsb.info.nih.gov/ij). Furthermore, semi-quantitative evaluation (ranged from 1 to 3) for histological changes (inflammatory infiltrate, alveolar hemorrhage, pulmonary edema, alveolar wall thickening, fusocellular proliferation, collagen accumulation and fibrosis in alveolar walls and interstitium) of the lung tissue was performed by a pathologist in a blinded fashion [57]. Global damage score corresponds to the sum of every histological change score.

4.13. Immunohistochemical analysis

Immunohistochemical staining was performed on formalin-fixed and paraffin-embedded tissue using the HRP staining method. Sections were cut 5-μm mounted on glass and dried overnight at 57 °C. All sections were then deparaffinized in xylene (2 × 5 min) and rehydrated through a graded series of alcohol (100%, 96%, 90%, and 70%) and distilled water. Subsequently, epitopes were retrieved: in the case of the IL-6 antibody, deparaffinized sections were boiled in EDTA buffer (pH 9), while for the rest antibodies, deparaffinized sections were boiled in citrate buffer (pH 6.0) at 97 °C for 20 min in a PT-Link instrument (Dako,

Glostrup, DK). Non-specific endogenous peroxidase reactivity was blocked with H_2O_2 reagent (ab64218, Abcam) for 30 min at room temperature (RT). Primary antibodies were incubated overnight at 4 °C. After washing, slides were incubated with the corresponding HRP secondary antibody at room temperature for 1 h. All required antibodies are listed in Supplemental Table 10. Tissue sections were revealed using 20 μL/mL DAB (Dako, Glostrup, DK) and counterstained with Carazzi's hematoxylin. Slides were mounted with MOWIOL (Calbiochem). Images were acquired by use of an Axio Imager.M1 (Zeiss microscope with a DMC6200 (Leica) digital camera Software LAS V.4.13. For each kidney, 10–15 fields were acquired with a 40X objective lens under transmitted light microscopy by using a DMC6200 digital camera (Leica AG, Heerbrugg, Switzerland) connected to an Axio Imager M1 Microscope (Zeiss AG, Jena, Germany), through the Leica Application Suite software (LAS v. 4.13). Staining quantification was assessed as stained area versus total analyzed area. It was performed blindly in an automated mode using the ImageJ 1.48 software (http://rsb.info.nih.gov/ij).

4.14. Pathway enrichment analysis

Single-cell RNA-seq data depicted in Supplemental Figs. 5A–C from Ref. [12] for alveolar type 1 and type 2 cells was explored via the data browsers at https://www.nupulmonary.org/covid-19/. Comparative gene enrichment analysis of the single-cell RNA-seq data depicted in Supplemental Figs. 5A–C from Ref. [12] (GEO: GSE155249) and from Supplemental Fig. 5D from Ref. [13] (GEO: GSE167747) was carried out using the corresponding gene sets for each pathway obtained from the R libraries KEGGREST (https://bioconductor.org/packages/release/bioc/html/KEGGREST. html, v1.36.3).

4.15. Clinical data

A cohort of 55 patients diagnosed with COVID-19 between March and June 2020, 15 of which had been on previous treatment with Metformin, from the University Hospital "Príncipe de Asturias" (Alcalá de Henares, Madrid) was evaluated for different clinical parameters (Supplemental Figures 1, 2 and **3**). Serum was obtained from all these patients, while BAL was obtained from 17 patients from this cohort. IL-6 and IL-1α levels in BAL samples were determined by ELISA (R&D Systems) according to the manufacturer's instructions. Clinical parameters from an additional cohort of 77 diabetic patients, 49 of which were on chronic treatment with Metformin, were also evaluated (Supplemental Figs. 4 and 5).

4.16. Statistical analysis

Data in experimental models were analyzed using nonparametric tests except where indicated. The difference between two independent groups was examined with Mann-Whitney test, while more than two groups were compared with Kruskal-Wallis test. The Chi-Square test was used to determine association between variables. In the pathway enrichment analysis, a two-sided Wilcoxon test was applied to check the expression differences between phenotypes. A P-value of 0.05 or less was considered statistically significant ($^{*/\#}$: $P < 0.05$, $^{**/\#\#}$: $P < 0.01$, $^{***/\#\#\#}$: $P < 0.001$). Data were analyzed using GraphPad Prism 6.0 (GraphPad Software, La Jolla, CA). Data are reported as mean ± standard error of mean (SEM).

Author contributions

SL conceived and directed research. VM designed, performed and analyzed the majority of experiments. CRS, JT, BS, EA, IR and LF performed experiments. JIH provided technical assistance for mouse experiments. CC performed histological evaluation. KCR, JJ, RK and DS provided intellectual insight and resources. LS and JMRGM collected information about COVID-19 patient cohorts. JN and IC performed bioinformatic studies. AC provided indol-based compounds. All authors helped with the discussion of the results and SL and VM wrote the manuscript.

Declaration of competing interest

The authors have no conflicts of interest.

Data availability

Data will be made available on request.

Acknowledgements

This work was supported by grants PID2019-104233RB-I00 and PID2022-136703OB-I00 funded by MCIN /AEI/10.13039/501100011033 / FEDER, Spanish National Research Council CSIC–COV19-096/ PIE202020E160, Comunidad de Madrid "NOVELREN" B2017/BMD-3751 and Fundación Renal "Íñigo Alvarez de Toledo", all from Spain. The CBMSO receives institutional support from Fundación "Ramón Areces". VM and EA hold a Juan de la Cierva-Formación fellowship from the Spanish Ministry of Science and Innovation (FJC2020-043505-I and FJC2021-046602-I, respectively). VM was supported by a Postdoctoral Long-Term Fellowship from the Federation of European Biochemical Societies (FEBS). CR and BS are recipients of a pre-doctoral fellowship of the FPI Program (BES-2016-076735 and PRE-2020-093831, respectively) from the Spanish Research State Agency. We thank the Servicio Interdepartamental de Investigación (SIdI) of the Universidad Autónoma de Madrid for its technical support with drug determinations as well as to the scientific and technical services of the CBMSO.

Appendix A. Supplementary data

Supplementary data to this article can be found online at https://doi.org/10.1016/j.redox.2023.102957.

References

[1] C.B. Jackson, M. Farzan, B. Chen, et al., Mechanisms of SARS-CoV-2 entry into cells, Nat. Rev. Mol. Cell Biol. 23 (2022) 3–20.
[2] D.A. Berlin, R.M. Gulick, F.J. Martinez, Severe covid-19, N. Engl. J. Med. 383 (2020) 2451–2460.
[3] N.J. Matheson, P.J. Lehner, How does SARS-CoV-2 cause COVID-19? Science 369 (2020) 510–511.
[4] D.C. Fajgenbaum, C.H. June, Cytokine storm, N. Engl. J. Med. 383 (2020) 2255–2273.
[5] J.S. Ayres, A metabolic handbook for the COVID-19 pandemic, Nat. Metab. 2 (2020) 572–585.
[6] I. Pernicova, M. Korbonits, Metformin–mode of action and clinical implications for diabetes and cancer, Nat. Rev. Endocrinol. 10 (2014) 143–156.
[7] J. Dai, K. Liang, S. Zhao, et al., Chemoproteomics reveals baicalin activates hepatic CPT1 to ameliorate diet-induced obesity and hepatic steatosis, Proc. Natl. Acad. Sci. U. S. A. 115 (2018) E5896–E5905.
[8] R.R. Reddel, Y. Ke, B.I. Gerwin, et al., Transformation of human bronchial epithelial cells by infection with SV40 or adenovirus-12 SV40 hybrid virus, or transfection via strontium phosphate coprecipitation with a plasmid containing SV40 early region genes, Cancer Res. 48 (1988) 1904–1909.
[9] G. Zhou, R. Myers, Y. Li, et al., Role of AMP-activated protein kinase in mechanism of metformin action, J. Clin. Invest. 108 (2001) 1167–1174.
[10] M. Sanz-Gomez, E. Aledavood, M. Beroiz-Salaverri, et al., Novel indolic AMPK modulators induce vasodilatation through activation of the AMPK-eNOS-NO pathway, Sci. Rep. 12 (2022) 4225.
[11] B.T. Thompson, R.C. Chambers, K.D. Liu, Acute respiratory distress syndrome, N. Engl. J. Med. 377 (2017) 562–572.
[12] R.A. Grant, L. Morales-Nebreda, N.S. Markov, et al., Circuits between infected macrophages and T cells in SARS-CoV-2 pneumonia, Nature 590 (2021) 635–641.
[13] J. Jansen, K.C. Reimer, J.S. Nagai, et al., SARS-CoV-2 infects the human kidney and drives fibrosis in kidney organoids, Cell Stem Cell 29 (2022) 217–231 e8.
[14] V. Miguel, J. Tituana, J.I. Herrero, et al., Renal tubule Cpt1a overexpression protects from kidney fibrosis by restoring mitochondrial homeostasis, J. Clin. Invest. 131 (2021).
[15] N.L. Price, V. Miguel, W. Ding, et al., Genetic deficiency or pharmacological inhibition of miR-33 protects from kidney fibrosis, JCI Insight 4 (2019).

[16] M. Merad, C.A. Blish, F. Sallusto, et al., The immunology and immunopathology of COVID-19, Science 375 (2022) 1122–1127.
[17] J.W. Lee, Y. Su, P. Baloni, et al., Integrated analysis of plasma and single immune cells uncovers metabolic changes in individuals with COVID-19, Nat. Biotechnol. 40 (2022) 110–120.
[18] E. Berber, D. Sumbria, S. Kokkaya, A metabolic blueprint of COVID-19 and long-term vaccine efficacy, Drug Metab Pers Ther 38 (2023) 15–29.
[19] P. Prasun, COVID-19: a mitochondrial perspective, DNA Cell Biol. 40 (2021) 713–719.
[20] A.L. Mora, M. Bueno, M. Rojas, Mitochondria in the spotlight of aging and idiopathic pulmonary fibrosis, J. Clin. Invest. 127 (2017) 405–414.
[21] A.S. Kulkarni, S. Gubbi, N. Barzilai, Benefits of metformin in attenuating the hallmarks of aging, Cell Metabol. 32 (2020) 15–30.
[22] G. Rena, D.G. Hardie, E.R. Pearson, The mechanisms of action of metformin, Diabetologia 60 (2017) 1577–1585.
[23] M. Foretz, B. Guigas, L. Bertrand, et al., Metformin: from mechanisms of action to therapies, Cell Metabol. 20 (2014) 953–966.
[24] T. Ma, X. Tian, B. Zhang, et al., Low-dose metformin targets the lysosomal AMPK pathway through PEN2, Nature 603 (2022) 159–165.
[25] D. Carling, AMPK signalling in health and disease, Curr. Opin. Cell Biol. 45 (2017) 31–37.
[26] Y. Li, X. Yang, P. Yan, et al., Metformin in patients with COVID-19: a systematic review and meta-analysis, Front. Med. 8 (2021), 704666.
[27] C.T. Bramante, J.B. Buse, D.M. Liebovitz, et al., Outpatient treatment of COVID-19 and incidence of post-COVID-19 condition over 10 months (COVID-OUT): a multicentre, randomised, quadruple-blind, parallel-group, phase 3 trial, Lancet Infect. Dis. 23 (2023) 1119–1129.
[28] S.M. Erickson, S.L. Fenno, N. Barzilai, et al., Metformin for treatment of acute COVID-19: systematic review of clinical trial data against SARS-CoV-2, Diabetes Care 46 (2023) 1432–1442.
[29] I. Sanchez-Cerrillo, P. Landete, B. Aldave, et al., COVID-19 severity associates with pulmonary redistribution of CD1c+ DCs and inflammatory transitional and nonclassical monocytes, J. Clin. Invest. 130 (2020) 6290–6300.
[30] X. Wang, G. Tang, Y. Liu, et al., The role of IL-6 in coronavirus, especially in COVID-19, Front. Pharmacol. 13 (2022), 1033674.
[31] T. Thomas, D. Stefanoni, J.A. Reisz, et al., COVID-19 infection alters kynurenine and fatty acid metabolism, correlating with IL-6 levels and renal status, JCI Insight 5 (2020).
[32] N. Wiernsperger, A. Al-Salameh, B. Cariou, et al., Protection by metformin against severe Covid-19: an in-depth mechanistic analysis, Diabetes Metab. 48 (2022), 101359.
[33] S. Rangarajan, N.B. Bone, A.A. Zmijewska, et al., Metformin reverses established lung fibrosis in a bleomycin model, Nat. Med. 24 (2018) 1121–1127.
[34] V. Kheirollahi, R.M. Wasnick, V. Biasin, et al., Metformin induces lipogenic differentiation in myofibroblasts to reverse lung fibrosis, Nat. Commun. 10 (2019) 2987.
[35] Y. Wang, H. An, T. Liu, et al., Metformin improves mitochondrial respiratory activity through activation of AMPK, Cell Rep. 29 (2019) 1511–15123 e5.
[36] L. He, F.E. Wondisford, Metformin action: concentrations matter, Cell Metabol. 21 (2015) 159–162.
[37] L. Console, M. Scalise, N. Giangregorio, et al., The link between the mitochondrial fatty acid oxidation derangement and kidney injury, Front. Physiol. 11 (2020) 794.
[38] H. Cui, N. Xie, S. Banerjee, et al., Impairment of fatty acid oxidation in alveolar epithelial cells mediates acute lung injury, Am. J. Respir. Cell Mol. Biol. 60 (2019) 167–178.
[39] H.M. Kang, S.H. Ahn, P. Choi, et al., Defective fatty acid oxidation in renal tubular epithelial cells has a key role in kidney fibrosis development, Nat. Med. 21 (2015) 37–46.
[40] H. Wang, Q. Jiang, L. Zhang, Baicalin protects against renal interstitial fibrosis in mice by inhibiting the TGF-beta/Smad signalling pathway, Pharm. Biol. 60 (2022) 1407–1416.
[41] E. de Boer, I. Petrache, N.M. Goldstein, et al., Decreased fatty acid oxidation and altered lactate production during exercise in patients with post-acute COVID-19 syndrome, Am. J. Respir. Crit. Care Med. 205 (2022) 126–129.
[42] S.T.R. Moolamalla, R. Balasubramanian, R. Chauhan, et al., Host metabolic reprogramming in response to SARS-CoV-2 infection: a systems biology approach, Microb. Pathog. 158 (2021), 105114.
[43] A. Valdes, L.O. Moreno, S.R. Rello, et al., Metabolomics study of COVID-19 patients in four different clinical stages, Sci. Rep. 12 (2022) 1650.
[44] I. Roberts, M. Wright Muelas, J.M. Taylor, et al., Untargeted metabolomics of COVID-19 patient serum reveals potential prognostic markers of both severity and outcome, Metabolomics 18 (2021) 6.
[45] J.E. Tanner, C. Alfieri, The fatty acid lipid metabolism nexus in COVID-19, Viruses 13 (2021).
[46] C. Lin, F.J. Tsai, Y.M. Hsu, et al., Study of baicalin toward COVID-19 treatment: in silico target analysis and in vitro inhibitory effects on SARS-CoV-2 proteases, Biomed. Hub 6 (2021) 122–137.
[47] J.H. Vernooy, M.A. Dentener, R.J. van Suylen, et al., Long-term intratracheal lipopolysaccharide exposure in mice results in chronic lung inflammation and persistent pathology, Am. J. Respir. Cell Mol. Biol. 26 (2002) 152–159.
[48] Y.J. Jung, Y.Y. Park, J.W. Huh, et al., The effect of human adipose-derived stem cells on lipopolysaccharide-induced acute respiratory distress syndrome in mice, Ann. Transl. Med. 7 (2019) 674.
[49] R.L. Chevalier, M.S. Forbes, B.A. Thornhill, Ureteral obstruction as a model of renal interstitial fibrosis and obstructive nephropathy, Kidney Int. 75 (2009) 1145–1152.
[50] M. Fink, M. Henry, J.D. Tange, Experimental folic acid nephropathy, Pathology 19 (1987) 143–149.
[51] P. Saz-Leal, C. Del Fresno, P. Brandi, et al., Targeting SHIP-1 in myeloid cells enhances trained immunity and boosts response to infection, Cell Rep. 25 (2018) 1118–1126.
[52] K.J. Livak, T.D. Schmittgen, Analysis of relative gene expression data using real-time quantitative PCR and the 2(-Delta Delta C(T)) Method, Methods 25 (2001) 402–408.
[53] F.K. Huynh, M.F. Green, T.R. Koves, et al., Measurement of fatty acid oxidation rates in animal tissues and cell lines, Methods Enzymol. 542 (2014) 391–405.
[54] G.J.W. van der Windt, C.H. Chang, E.L. Pearce, Measuring bioenergetics in T cells using a Seahorse extracellular Flux analyzer, Curr. Protoc. Im. 113 (2016) 3 16B 1–3 B 4.
[55] S. Ravi, B. Chacko, P.A. Kramer, et al., Defining the effects of storage on platelet bioenergetics: the role of increased proton leak, Biochim. Biophys. Acta 1852 (2015) 2525–2534.
[56] J. Varga, D.A. Brenner, S.H. Phan, Fibrosis Research: Methods and Protocols, Springer Science & Business Media, 2008.
[57] S. Tian, Y. Xiong, H. Liu, et al., Pathological study of the 2019 novel coronavirus disease (COVID-19) through postmortem core biopsies, Mod. Pathol. 33 (2020) 1007–1014.